Exploring laser-induced cavitation for primary nucleation control

An experimental study

Aswin Raghunathan

Technische Universiteit Delft

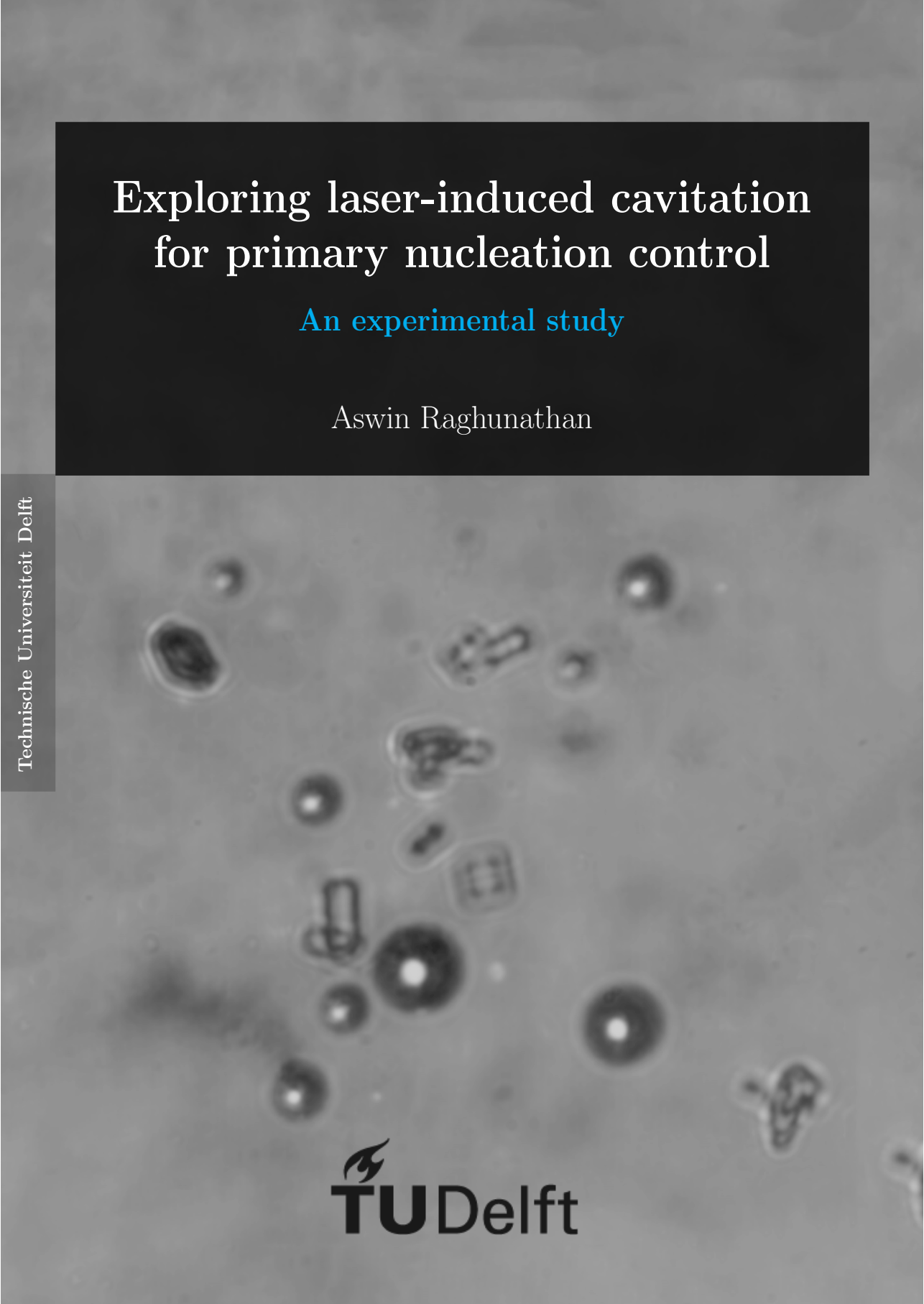

TU Delft

EXPLORING LASER-INDUCED CAVITATION FOR PRIMARY NUCLEATION CONTROL

AN EXPERIMENTAL STUDY

by

Aswin Raghunathan

to obtain the degree of Master of Science
at the Delft University of Technology,
to be defended publicly on Monday May 30, 2022 at 12:30 P.M.

Student number:	5128188	
Project duration:	July 19, 2021 – May 30, 2022	
Thesis committee:	Prof. dr. ir. J. T. Padding,	TU Delft, chairman
	Dr. ir. H. B. Eral,	TU Delft, supervisor
	Dr. ir. W. P. Breugem,	TU Delft
	Ir. N. Nagalingam,	TU Delft, daily supervisor

An electronic version of this dissertation is available at
http://repository.tudelft.nl/.

TU Delft

"Nothing in life is to be feared, it is only to be understood
Now is the time to understand more, so that we may fear less."

—

Marie Sklodowska Curie
(1867–1934)

PREFACE

The thesis marks the completion of the required credits in order to obtain the degree of Masters in Mechanical Engineering under the track 'Energy, Flow and Process Technology'. The research was carried out at the Erallab in the department of Process and Energy (P&E, 3mE) under the supervision of Dr. ir. Burak Eral. The report aims to summarize the work done in studying the effect of laser-induced cavitation on the formation of crystals in supersaturated aqueous solutions using confined and unconfined microfluidic systems.

This report provides a detailed documentation of the literature reviewed to understand the technical background of the problem, experimental campaign and the results, discussions and conclusions obtained from the experiments. The readers interested in getting an overview of laser-induced crystallization are directed to read the chapter 1. Based on the interests of the readers, those who are trying to reproduce a similar working setup are directed to chapter 2 and appendices A, B and C. Whereas those who are interested in the experimental results obtained from confined and unconfined geometries are directed to chapters 3 and 4 respectively.

I take the full responsibility for the contents published in this report, be it the clarity on the structure or the subject addressed. Constructive criticisms on any part of the work can be put forth to the author as they would be received in a good way for self-improvement. At the moment, further experiments are being carried out to expand the generated phase map for nucleation probability. In addition, experiments are in progress as to increase the number of existing trials for better statistical accuracy.

The cover page indicates the formation of bubbles and crystals after a solution of supersaturated aqueous potassium chloride–potassium permanganate is irradiated using a single nanosecond laser pulse. The image is taken from the experiments performed in the present work.

Aswin Raghunathan
Delft, May 2022

ACKNOWLEDGEMENTS

This section of the report is dedicated to the incredible people that I have been associated with during the past few years and without whom it wouldn't have been possible to complete this part of my journey in life.

First off, I would like to take this opportunity to thank **Dr. Burak** for providing me the opportunity to pursue this research on not just a challenging topic on it's own merit but also with high relevance to the industrial applications. The freedom provided by you during the research work, your insights and critical attitude while looking at the results and, above all, offering valuable advice on improving my communication skills during the progress meetings will never be forgotten. Next up, I tip my hat to my daily supervisor **Nagaraj** who introduced me to this wonderful topic and has always been there on my side offering considerable help during several stages of my research. I would like to specially thank the committee members **Dr. Johan** and **Dr. Wim-Paul** for being very considerate with the graduation formalities and taking time out of their busy schedule to read my thesis and attend my master defence.

I would like to express my gratitude towards a number of people that have chipped in during the development stages of the experimental setup. I'm grateful to **Edwin** for all the help and knowledge that was provided on the optics part with regards to imaging and laser and more importantly, allowing to borrow the laser and cameras whenever it was needed. I would also like to add some words of appreciation to **Michel** and the other lab technicians for providing assistance in acquiring and relocating different parts that were useful for my working setup. I would also like to extend my gratitude to all the people from the NLPIN research group who have helped with several things at different phases of my research. I would like to convey my regards to **Dr. Herman** and **Dr. Antoine** for giving useful inputs and suggestions during the experimental campaign. A big thanks to **Vikram** for aiding me in both technical and practical aspects of the project and not to forget, the occasional exchanges of each others' worries which acted as a stress buster at many times. A big shout out to all the fellow master students **Haripriya**, **Mias** and **Xiuzi** who have assisted me with answering my doubts and providing useful suggestions along the way.

Stepping into my student's shoes, I'm thankful to all my friends in Delft – **Ravi**, **Shyam**, **Sneha** and **Venkat**, in specific, who have been hugely supportive during the course of my study, not just while working with assignments but also while spending some quality time roaming around the city, cooking together and much more, especially during the difficult times with lockdowns due to the COVID pandemic. A special mention goes out to **Shravan** who has offered me invaluable help starting from the early days of coming here to study even up until today.

Reflecting on my overall growth up until this point, I will forever be indebted to all my **Gurus** (teachers) who have imparted knowledge and have inscribed good virtues in me throughout my entire life, for whom I dedicate this work. Finally, no words can be enough to describe the sacrifices made and the love and support offered by my **parents** and my **sister** all through my life and especially during the past couple of years which have undoubtedly been the longest and the hardest time ever being outside of home, as yet.

अंतः अस्ति प्रारंभः

‖ Antaha asti praarambhaha
The end is the beginning ‖

Aswin Raghunathan
Delft, May 2022

ABSTRACT

Crystallization is one of the most sought after separation and purification technique in the process industries. However, the fundamental understanding on the formation of crystals poses quite a challenge due to the inherent complexity and stochasticity associated with the process. In the past, several attempts put forth to control crystal nucleation have been anything but successful. But, more recently, the use of lasers to control primary nucleation have led to promising prospects.

In the current study, efforts were made to explore the phenomena behind Non-Photochemical Laser Induced Nucleation (NPLIN). Experiments were carried out starting with a confined microfluidic system for both supersaturated aqueous potassium permanganate and potassium chloride solutions and later extended to unconfined geometry with potassium chloride solutions. A single nanosecond laser pulse of 532 nm wavelength was employed to create vapour bubbles and the resulting crystal formation was quantified.

To begin with, a quadratic relationship between the laser energy supplied and the maximum radius of the bubble formed was observed. By systematically varying both the supplied laser energy and the solution supersaturation, the probability of crystal formation for various energy–supersaturation combinations were studied. A minimum laser energy threshold for crystal formation was observed to be a function of solution supersaturation. The results obtained in this study will aid in developing a numerical model that can apriori predict the minimum necessary laser and supersaturation conditions required for any given salt to undergo NPLIN.

Keywords: NPLIN, microfluidics, laser-induced cavitation, crystallization and experiments.

CONTENTS

List of Figures

List of Tables

1

INTRODUCTION

> *The only limit to our realization of tomorrow will be our doubts of today.*
>
> Franklin D. Roosevelt, *1882–1945*

> *Crystallization is still referred to as more of an art than a science. There is undoubtedly some truth in this old adage, but it cannot be denied that there is a considerable amount of science associated with the art.*
>
> John Mullin, *Crystallization*, *1960* [1]

Crystallization is the process of phase transition by which a pure crystalline solid state product is obtained from a solution or a melt. It is one of the oldest and cheapest unit operation that is employed both as a separation as well as a purification method [1]. A large number of small scale and large scale chemical industries employ this process to produce the required intermediate and final products. The widespread importance of crystallization spans across various domains which mainly includes but not limited to the pharmaceutical, agrochemical, fine chemical, petrochemical, animal health and food industries [2]. Although, crystallization is being carried out for several decades and has grown to be one of the most increasingly significant industrial processes, the underlying mechanism behind the formation of crystals is still very poorly understood. This is mainly because of the several complexities that governs the process involving the thermodynamics of phase transformation, reaction kinetics and the associated transport phenomena [3].

As there are many factors that intertwine within the crystallization process, the production of good quality crystals in terms of their size distribution, polymorphic forms, morphology and purity largely rely on trial and error at present. Therefore, it is imperative to understand the physical processes that occur in order to obtain a better control over the process.

1

1.1. FUNDAMENTALS OF CRYSTALLIZATION PROCESSES

1.1.1. SUPERSATURATION AND SOLUBILITY DIAGRAM

The first step in order to generate crystals is the presence of a supersaturated solution. *Supersaturation* is the main driving force for crystallization to occur. In simple terms, it is defined as the difference between the chemical potential of a solute and the chemical potential that the solute will exert under equilibrium conditions. For a given temperature, supersaturation of a solution is expressed as follows,

$$S = \frac{c}{c_{\text{sat}}} \tag{1.1}$$

where S is the supersaturation, c is the solute concentration and c_{sat} is the saturation concentration corresponding to the solution temperature.

In spite of the fact that a supersaturated solution is thermodynamically unstable, crystallization may not occur spontaneously. Based on the nature of external perturbation, this process might happen over a period of several minutes to even several years [4]. A *solubility–supersolubility diagram* is used to portray the relationship between supersaturation and spontaneous crystallization. A typical solubility–supersolubility diagram is depicted as shown in Figure 1.1.

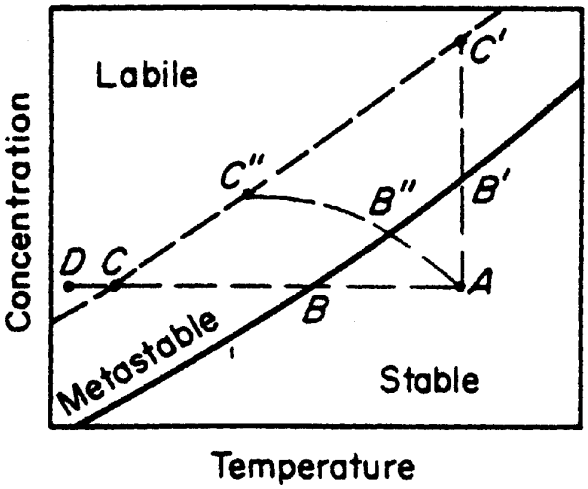

Figure 1.1: A solubility–supersolubility diagram indicating different states of a concentrated solution. Solid line represents the solubility curve of a compound and the dotted line in parallel represents the ill-defined supersolubility curve. Figure reproduced from Mullin [1].

This plot is primarily divided into three regions namely stable, metastable and labile. In the stable region, the solution is undersaturated and thereby crystallization is not possible. In the metastable region, crystallization does not occur spontaneously but through crystal seeding or other external influences such as shock, agitation, ultrasound or laser [1]. In the labile region, crystallization occurs spontaneously but not inevitable. Crystallization can

be achieved either by cooling down the solution preventing mass transfer (curve ABC) or by evaporation of solvent from the solution at a given temperature (curve AB'C') or both simultaneously (curve AB"C").

1.1.2. NUCLEATION

Even though, supersaturation is a necessity for crystallization to happen, it is not adequate for a system to form crystals as it requires active centres such as nuclei to develop and grow subsequently. *Nucleation* is the physical process that leads to the emergence of a new phase of a substance. It is mainly classified into two types: primary and secondary nucleation. In primary nucleation, the formation of the new phase takes place spontaneously (homogeneous nucleation) or due to the foreign particles induced in the solution such as impurities (heterogeneous nucleation). Whereas in secondary nucleation, the parent crystals of the same solute are added as seeds in the solution to enhance crystal formation. The mechanism of primary nucleation is not very well known but is described to a certain extent using two generic models, i.e., *Classical Nucleation Theory* (CNT) and *Two-Step Nucleation model* (TSN).

CLASSICAL NUCLEATION THEORY

Following the works of Gibbs, Volmer, Becker and Döring and others, the CNT was originally applied for condensation of a vapour into a liquid and later analogised to systems that undergo crystallization from supersaturated solutions [5]. According to this theory, small solute clusters are formed in the metastable region prior to the occurrence of primary nucleation. The overall free energy change (ΔG) associated with the formation of these clusters is the summation of the free energy change associated with the formation of surface (ΔG_S) and the free energy change associated with the phase change (ΔG_V). As solid state is more thermodynamically favourable due to its lower chemical potential compared to liquid, the volume free energy ΔG_V always decreases. On the other hand, creation of new solid particles in the solution amounts to increase in surface area which results in the increase of surface free energy ΔG_S. Thus, the evolution of these nucleation clusters depends on the balance between the increasing ΔG_S which promotes dissolution and the decreasing ΔG_V which promotes growth. The energy trend representation of this concept is provided in Figure 1.2.

The overall free energy change can be expressed using an equation as shown below.

$$\Delta G = \Delta G_S + \Delta G_V = 4\pi r^2 \gamma + \frac{4}{3}\pi r^3 \Delta G_v \tag{1.2}$$

where r is the radius of the cluster, γ is the interfacial tension between the emerging solid surface and the solvent and ΔG_V is the free energy change of the phase transformation per unit volume.

At the starting point, when the size of the nuclei cluster is much smaller, the surface energy dominates leading to an increase in the overall free energy. As the cluster size increases above a critical point (r_c), the total free energy overcomes a maximum value (ΔG_{crit}) upon which it starts to decrease as the crystal growth becomes energetically favourable.

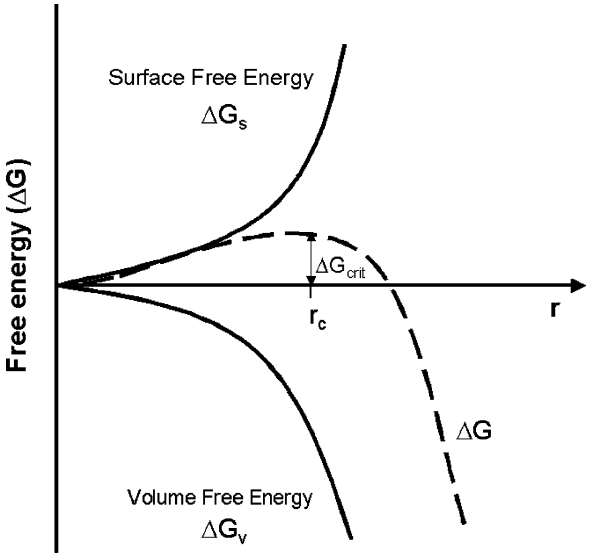

Figure 1.2: A schematic representation of the free energy barrier to nucleation arising from the CNT. ΔG_{crit} denotes the maximum total free energy required to be overcome for the formation of a stable nuclei and r_c denotes the critical cluster radius. Figure reproduced from Erdemir et al. [5].

TWO-STEP NUCLEATION

Since, the CNT is a very simplistic model that is based on several basic assumptions, there are numerous setbacks when it comes to explaining certain complex processes such as nucleation in binary mixtures. Due to the difference in composition of the clusters in such mixtures causing surface enrichment effects, the CNT fails to predict the nucleation rates both qualitatively and quantitatively [5]. Based on these observations and a series of experiments and molecular dynamics simulations performed over the subsequent years, an alternative approach known as the TSN model was proposed. According to this mechanism, nucleation is considered as a two-barrier process where a liquid-like droplet is created as a precursor to the formation of amorphous clusters which further reorders to form crystalline clusters. In theory, the free energy change required for the first step is lower than that of the main energy barrier that needs to be overcome for the nucleus to sustain its growth. A schematic representation of the two primary nucleation mechanisms is presented in the Figure 1.3.

However, the aforementioned theories can only elucidate nucleation to some degree of certainty, there is still more work to be done in terms of understanding the subject and establishing a strong theoretical and mathematical framework. In addition to this, the stochastic nature of primary nucleation makes it even more harder to study it as there is no assurance that crystals will be formed even though the exact thermodynamic conditions for nucleation are met. In the past, a lot of different techniques have been developed to induce nucleation by external means such as mechanical shocks [6, 7], agitation and fluid shear [8–11], application of high pressures within the solutions [12], electric fields [13, 14],

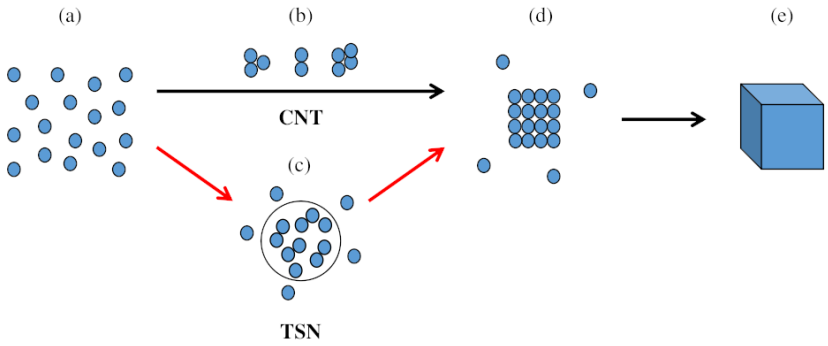

Figure 1.3: A graphical illustration of the two nucleation mechanisms: (a) distribution of solute molecules in the supersaturated solution; (b) ordering of pre-critical solute clusters; (c) formation of liquid-like droplet housing the amorphous solute clusters; (d) structural rearrangement to form crystalline nuclei and (e) final product crystal. Figure adapted from Ward [4].

Ultraviolet (UV) rays, X-rays and γ-rays [1], high intensity ultrasound or sonocrystallization [15, 16] and, of late, laser irradiation [17] albeit achieving no success in expanding these methods to the industrial scales as yet.

1.2. NON-PHOTOCHEMICAL LASER INDUCED NUCLEATION: A LITERATURE REVIEW

Over the last decade, there has been an increasing interest to study nucleation induced by laser irradiation due to its overwhelming potential when compared to the other existing methods. When a nanosecond pulsed laser is passed through a supersaturated aqueous solution, crystals are observed to be formed instantaneously. This method of crystallization is referred to as *Non-Photochemical Laser Induced Nucleation* (NPLIN). The term non-photochemical is coined based on the fact that the solution does not undergo any physical or chemical transformation due to the laser as there is no light absorption at the irradiated wavelengths (λ = 532/1064 nm) and laser intensities (~MW/cm^2) [18]. NPLIN has recently gained more attraction mainly because of its ability to provide remarkable control over the nucleation process both spatially and temporally based on the laser beam's shape, size, path and the pulse duration [19]. An example of a typical NPLIN experiment using a small glass vial filled with a supersaturated solution of potassium chloride in water is shown in Figure 1.4.

1.2.1. DISCOVERY OF NPLIN

NPLIN was discovered accidentally by Garetz et al. [17], when supersaturated aqueous solution of urea was subjected to the pulses of Q-switched Nd:YAG laser while aiming to observe second harmonic generation. A plane-polarised laser beam with a wavelength of 1064 nm and pulse duration of 20 ns was employed to one or two week aged urea solutions with supersaturations ranging from 1.1 to 1.29. Under normal conditions, these solutions remained for several weeks before nucleating but as soon as the laser was irradiated

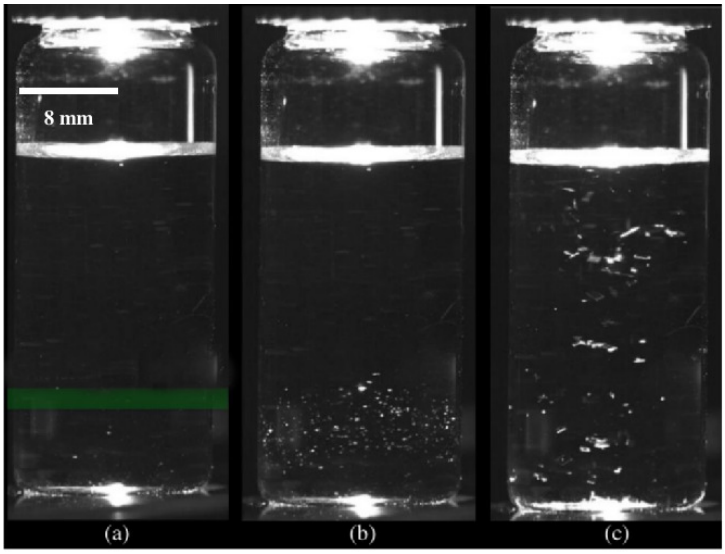

Figure 1.4: Demonstration of NPLIN in a 3 ml glass vial containing supersaturated aqueous potassium chloride solution irradiated with a single laser pulse (7 ns, 532 nm). Images are depicted at times: (a) t = 0 s; (b) t = 1 s and (c) t = 5 s after laser irradiation. The path of the laser beam is marked in green. Figure adapted from [20].

spontaneous nucleation was observed. Since, urea in water is transparent to 1064 nm laser, multiphoton absorption of light was ruled out as the possible cause. As the needle-shaped crystals that were observed oriented themselves in a preferred direction, they claimed it to be an effect of the externally induced electric field due to the laser. Following this discovery, solutions of different compounds were studied using different laser properties that led to a number of experimental observations which are listed in the following section.

1.2.2. OBSERVATIONS FROM PREVIOUS NPLIN EXPERIMENTS

Over the last two decades, several NPLIN experiments have been performed and a number of experimental observations were recorded in order to shed some light on the mechanism behind NPLIN. Some of the important observations in the context of this study are listed as follows:

- NPLIN has been observed in a broad range of systems such as alkali metal halides [21], small molecules [22] and organic compounds [23–25], single component systems [26, 27] and dissolved gases [28, 29]. However, it is also worthy to note that not all systems were reported to undergo NPLIN, for instance, Acetamide [30] to which the reason remains unknown till date.

- Nucleation probabilities were observed to increase significantly due to increase in the supplied peak laser intensities and bulk supersaturation of the solution [31–33], whereas nucleation probability was found to be independent for different laser wavelengths [34].

- Crystal nucleation was reported to be induced by a single pulse of laser [21, 32, 34] but the pulse duration in order of femtoseconds was observed to be insufficient to trigger nucleation in several systems such as carbondioxide gas, potassium/ammonium chloride and urea solutions as compared to nanosecond pulses for the same peak laser power intensity (28 MW/cm^2) [30].

- The peak laser intensity was reported to linearly increase with the number of crystals observed for supersaturated solutions of potassium chloride and glycine [35, 36]. Whereas, for a system with carbonated solution, a quadratic increase in the number of carbondioxide gas bubbles was observed [29].

- Nucleation was reported to not occur below a minimum laser energy threshold [32]. However, the reason for the existence of such a threshold remains to be vindicated.

- The nucleation probabilities were found to be improved by aging the solutions in the case of glycine [22] and urea [17]. In spite of that, the nucleation probabilities of alkali metal halides were observed to remain invariant due to aging [32].

The aforementioned observations and key points highlight that the exact underlying mechanism (or mechanisms) for NPLIN is still an open question. Some probable mechanisms for NPLIN were suggested based on these experimental observations which are discussed briefly in the upcoming sections.

1.2.3. OPTICAL KERR EFFECT

In order to delineate the observations of NPLIN in supersaturated aqueous urea solutions, the *optical Kerr effect* (OKE) was initially put forth by Garetz et al. [17]. According to this hypothesis, an external electric field produced due to the laser induced a dipole moment that provided a torque which aligned the anisotropically polarizable molecules with its most polarizable axis parallel to the incident laser light, i.e., in the direction parallel to the applied electric field. As a result, the free energy barrier for nucleation was claimed to be lowered due to the reorientation of these existing pre-critical solute clusters in the presence of the electric field. The different steps in the formation of crystal as per the OKE mechanism is portrayed in Figure 1.5.

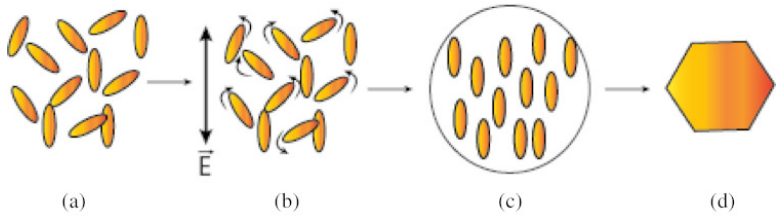

Figure 1.5: A schematic illustration of the OKE mechanism: (a) random distribution of the solute molecules; (b) torque applied on the solute molecules due to the laser-induced electric field; (c) orderly arrangement of the solute molecules in the cluster and (d) formation of solid crystal. Figure reproduced from Sanjana [37].

However, Matic et al. [33], through simple analytical calculations, identified that the computed induced dipole interaction energy for the urea molecules was several orders of magnitude smaller to account for this reduction in nucleation time and further suggested that the collective effects of many solute molecules in a big cluster could probably account for this disparity. In view of this, Knott et al. [38] performed Monte Carlo simulations using Potts lattice gas model to examine the effect of this rearrangement of solute molecules in reducing the energy barrier for nucleation. They reported that this orientational bias promoted nucleation of these large sub-critical solute clusters only at electric field strengths much greater than those employed in the NPLIN experiments. Furthermore, OKE cannot explain the mechanism of NPLIN in metal halides such as potassium chloride [32] or potassium bromide [21] as these compounds exists as ions within the solution and do not have a preferred orientation direction under laser irradiation. This implied that the OKE concept was not entirely sufficient to explain the mechanism behind NPLIN.

POLARIZATION SWITCHING

Polarization switching (PS) has hitherto been one of the foremost evidence that reinforces the existence of OKE. According to this mechanism, a change in polarization of laser light leads to a change in the polymorph of a compound. Polymorphism, which describes the existence of more than one crystal structure for a given chemical compound, is one of the most important phenomena in industrial crystallization [39]. The difference in the lattice structures that depend on the arrangement of the molecules leads to significant changes in the physical and chemical properties of a substance which is exploited by many chemical process industries for numerous applications. Although, polymorphism is being investigated for more than a century, prediction and control of the desired polymorphs still remains a daunting challenge [40].

One of the initial NPLIN experiments with organic compounds were performed by Zaccaro et al. [22]. They observed that the amino acid glycine in water produced a γ-polymorph despite the fact that a more stable α-polymorph is formed during spontaneous nucleation. From the existing literature, glycine is very well known to exhibit three polymorphs under different conditions namely α, β and γ-glycine [41]. Further investigation by Garetz et al. [42] resulted in the very first evidence of the PS mechanism wherein the linear and circular polarizations of the incident laser light gave rise to γ and α-glycine polymorphs respectively. This effect was interpreted in terms of structural motifs of the polymorphs indicating that the alignment of chains of molecules differed based on the laser light polarization change which appeared to go hand in hand with the theory behind OKE mechanism. Thereafter, similar observations were made on the effect of laser polarization on polymorphism control for other organic compounds such as L-Histidine [23], sulfathiazole [24] and carbamazepine [25]. In spite of that, more recent experiments performed by Liu et al. [31] reported that the polymorph shift from α to γ-glycine while using linearly polarized light occurred within a limited supersaturation range (S = 1.46 – 1.55) whereas Irimia et al. [43] couldn't reproduce the results for glycine under similar experimental conditions making the validity of this mechanism more questionable.

1.2.4. DIELECTRIC POLARIZATION

As the NPLIN of certain metal halides cannot be explained by the OKE mechanism, Alexander et al. [32] came up with a new hypothesis known as the *dielectric polarization* (DP) mechanism to explain NPLIN in aqueous potassium chloride solutions. The DP model, which provides a quantitative framework from the experimental results established on the foundations of CNT, is based on the isotropic electronic polarizability of potassium chloride clusters. In a static electric field, the free energy barrier to nucleation is set to be minimized when a homogeneous dielectric particle is immersed in a dielectric medium. However, this is applicable only when the dielectric constant of the particle, i.e., the solute potassium chloride (ϵ_p) is higher than that of the dielectric medium, i.e., the solvent water (ϵ_s), in this case. The theoretical basis of CNT described by Eqn. 1.2 can be extrapolated to account for the effect of laser-induced electric field as follows.

$$\Delta G = 4\pi r^2\gamma + \frac{4}{3}\pi r^3(\rho k_B T \ln S + aI) \tag{1.3}$$

where ρ is the number density of solute cluster, k_B is the Boltzmann constant, T is the temperature of the solution and S is the solution supersaturation. In this case, the free energy change for the phase transformation is assumed to be contributed by both the difference in chemical potential as well as the electric flux density due to laser irradiation. The effective dielectric constant (a) and the laser intensity (I) is defined as shown below.

$$a = \frac{3\epsilon_s}{c}\left(\frac{\epsilon_p - \epsilon_s}{\epsilon_p + 2\epsilon_s}\right) \tag{1.4}$$

$$I = \frac{1}{2}c\epsilon_0 E^2 \tag{1.5}$$

where ϵ_0 is the vacuum dielectric permittivity, ϵ_p is the relative permittivity of solute, ϵ_s is the relative permittivity of solvent, c is the velocity of light and E is the electric flux.

Following this modified classical nucleation model, Ward et al. [21] derived a relation to estimate the probability of nucleation (number of observable crystals in the solution), $p_n = 1 - \exp\{(-mI)\}$ assuming a Poisson distribution for fitting the experimental data where m is the laser intensity-independent *lability* computed theoretically as,

$$m = \frac{3N_{mol}\gamma a}{2\pi\rho^3(k_B T \ln S)^2} \times \frac{e^{-\Delta G_{crit}/k_B T}}{\int_0^{r_c} r^3 e^{-\Delta G/k_B T} dr} \tag{1.6}$$

where N_{mol} is the total number of solute molecules in the laser irradiated volume of the solution.

From the initial experiments performed in aqueous potassium chloride solutions, Alexander et al. [32] noticed that a minimum laser threshold intensity (I_0) was required to nucleate the samples. In order to account for this, the nucleation probability was corrected such that $p_n = 1 - \exp\{[-m(I - I_0)]\}$. The variation in the nucleation probabilities for varying laser intensities above the threshold in supersaturated aqueous potassium chloride solution is represented in Figure 1.6. It can be noticed that the prediction of nucleation probability

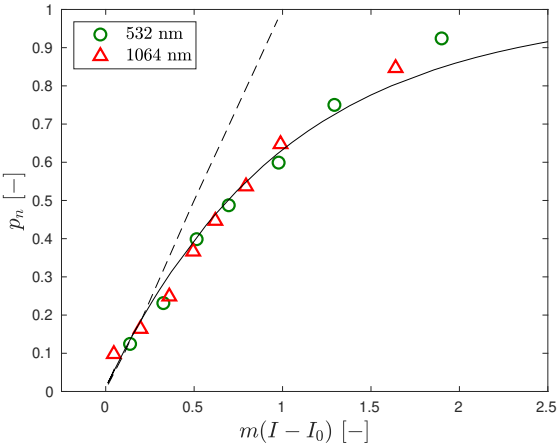

Figure 1.6: Nucleation probabilities of aqueous potassium chloride solution (S = 1.06) as a function of laser intensity expressed as $m(I - I_0)$ for two different laser wavelengths. Solid line represents the DP model prediction and dashed line represents the linear dependence. Figure adapted from Alexander et al. [14].

according to the DP model agreed well with the experimental data and a linear dependence can be established for the values that lie closer to the laser intensity threshold. However, the existence of this intensity threshold cannot be rationalized using the DP model. Furthermore, for higher energy intensities, the dependence of polarization and wavelength on the nucleation probability from the experiments with aqueous urea solutions as observed by Matic et al. [33] and the polymorph control of glycine under different polarizations as observed by Garetz et al. [42] could not be explained by the DP model.

1.2.5. NANOPARTICLE HEATING

Nanoscale particles are ubiquitous in nature and their heat transfer characteristics have been studied for their wide-ranging applications especially in the field of bio-medicine [44]. These nanoparticles or nano-impurities inherently present in the solution are known to absorb the irradiated laser light depending on their size and shape. The *nanoparticle heating* (NPH) relies on the fact that the nano-impurities existing in the solution can trigger nucleation on interaction with laser light. According to this hypothesis, the heat absorbed by the nano-impurity is dissipated into the solution locally surrounding the particle. This heat causes evaporation of the solvent in the vicinity of the impurity leading to the formation of a vapour bubble. The high rate of evaporation at the vapour–liquid interface of the bubble during its growth is expected to trigger an increase in the local supersaturation and thereby enhancing the possibility for crystal nucleation. This hypothesis is in accordance with the proposed mechanism by TSN model. The sequential steps involved in the formation and growth of a vapour bubble is represented in Figure 1.7.

This hypothesis was initially proposed by Ward et al. [29] while carrying out laser-induced nucleation in carbonated sugar solutions. When a single pulse of 532 nm wavelength and

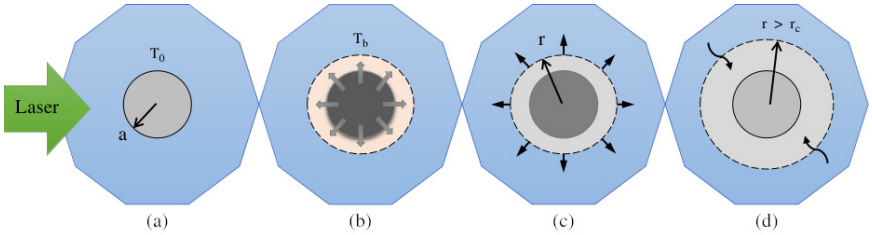

Figure 1.7: A graphical representation of the NPH mechanism: (a) laser absorption by nano-impurity of radius a in a solution at an ambient temperature of T_0; (b) heat dissipation to the surrounding liquid that starts to vaporize upon reaching the boiling temperature T_b; (c) radial vapour bubble expansion and (d) Continued expansion of vapour bubble leading to the formation of crystals when the bubble radius r exceeds the critical radius r_c. Figure adapted from Ward et al. [29].

5 ns pulse duration from a Nd:YAG laser was passed through a vial containing sucrose solutions supersaturated with carbondioxide gas, they noticed the formation of many small micro-sized bubbles in the path of the laser beam similar to NPLIN of crystals in metal halides. They also observed a threshold energy intensity of about $4.8\,\mathrm{MW/cm^2}$ for the formation of bubbles which happened to be in the same ball park as the threshold for NPLIN of supersaturated aqueous potassium chloride ($6.4\,\mathrm{MW/cm^2}$). Furthermore, they observed that filtered sucrose solutions produced significantly lesser bubbles than unfiltered solutions which emphasizes the influence of nano-impurities in nucleation.

In order to investigate the effect of nano-impurities on crystal nucleation in specific, Ward et al. [30] compared the filtered and unfiltered solutions of aqueous ammonium chloride and spotted a striking difference in the nucleation probabilities. They inferred that the unfiltered solutions yielded more number of nuclei per sample when compared to filtered solutions. Additionally, introducing doped iron oxide nanoparticles resembling the nano-impurities deliberately into the filtered solutions produced a similar nucleation probability as unfiltered solutions and upon adding a surfactant which is expected to disperse the impurities homogeneously in the solution produced the highest nucleation probability relative to all the other cases.

This shows the potential of the NPH mechanism to explain the existence of the laser energy intensity threshold observed in the NPLIN experiments based on the critical size of the bubble necessary to induce nucleation. The evolution of the bubble indirectly relates to the variation in local supersaturation surrounding the bubble in order to promote nucleation and growth of crystals.

1.3. MOTIVATION AND RESEARCH QUESTIONS

The present work is mainly focused on understanding the mechanism behind NPLIN. While there are several studies that have been performed thus far, there is still a lack of understanding and insufficient information in the literature with regards to this. At this juncture, the addition of valuable data to this field of research in order to expand the existing knowledge on NPLIN serves as the motivation to pursue the current study.

The primary focus of this study is to understand the mechanism of NPH as it has the potential to explain most of the observations that have been documented so far. In this work, we consider an idealized case of NPH where we intentionally form a vapour bubble by heating the solution using a focused laser beam. Due to the numerous possible parametric dependencies of NPLIN with respect to the laser, the current study is limited to investigating the effects of a single nanosecond laser pulse of 532 nm wavelength. It is hypothesized that the evaporation of solvent in the vicinity of the vapour–liquid interface along with the reduction in temperature of the solution locally after the laser irradiation leads to an increase in supersaturation which is believed to play an essential role in inducing crystal nucleation [45].

In this regard, having established the overview of previous research and identifying the gaps in literature, the general overarching research questions of this study are as follows:

1. Is laser-induced cavitation a viable mechanism for NPLIN?

2. Does the increase in local supersaturation at the vicinity of vapour bubble interface due to solvent evaporation serve as the main driving force for primary nucleation?

3. Under the given conditions such as supersaturation and laser intensity, is it possible to predict if a compound can undergo NPLIN or not?

Within the purview of the above generalized research questions, we introduce the following as the primary research objectives of the study:

- To investigate the relationship between the supplied laser energy and the maximum size of the bubble formed

- To explore the effects of laser energies on the nucleation probabilities by varying bulk supersaturation of the solution

1.4. RESEARCH GOALS

In order to seek answers to the aforementioned questions, the following are the main goals or the desired plan of action for this study:

- Design, develop and test an experimental setup to study the dynamics of the vapour bubble formation, growth and collapse

- Repeat the above experiments in a supersaturated aqueous salt solution in order to check for the formation of crystals

- Investigate the effect of laser intensity and supersaturation on the nucleation probability

1.5. ORGANIZATION OF THE REPORT

This section provides a general guide to this thesis. In the introduction chapter, the fundamentals of crystallization and a brief overview of NPLIN is provided along with describing some of the key experimental observations accompanying the hypothesized mechanisms. In the final part of this chapter, the motivation to pursue the current work and the goals of this study are discussed. The second chapter provides a detailed description of the experimental setup employed in this work together with components used in the setup, different geometries with which the experiments were performed, preparation of sample and studying the solubility curves of the compounds used. In the third chapter, experiments performed in micro-capillaries with three different solutions are discussed. The results obtained and the difficulties that were faced during the experimental campaign are also discussed briefly. The fourth chapter deals with the experiments performed in a cubic well geometry. A part of the chapter addresses the dynamics of the cavitation bubbles that are formed after the laser impact whereas the second half discusses about the aspects of crystallization in supersaturated solutions probing more into nucleation probabilities along with some overall observations from the experiments conducted. Finally, the major conclusions reached during this study are discussed in the last chapter and further recommendations to extend this research are also presented.

2

EXPERIMENTAL METHODOLOGY

> *If science is to progress, what we need is the ability to experiment. It is the facts that matter, not the proofs. Physics can progress without the proofs, but we can't go on without the facts.*
>
> Richard P. Feynman, *1918–1988*

This chapter discusses, in detail, the components used in the experimental setup, specifics of the geometries used, materials and sample preparation routine and methodology employed to systematically gather and study the observations in the current work. A microfluidic setup is developed in order to observe and study the dynamics of the cavitation bubble during its formation, growth and collapse and thereafter the crystal formation and its growth in supersaturated aqueous salt solutions. In comparison to the conventional batch processes performed with crytallizers or typical laboratory experiments performed with millimeter-sized glass vials, microfluidics present several advantages such as good control over the process, ideal heat and mass transfer, minimization of material use and wastage and reduction in contamination of the samples [36].

2.1. EXPERIMENTAL SETUP

An outline of the experimental setup is shown in Figure 2.1. Cavitation bubbles in the solution are generated using a 532 nm pulsed Nd:YAG laser (Nano L 50–50 PIV, Litron, Warwickshire, UK) with a pulse duration of 4 ns. The laser beam path is guided from the laser source using fully reflecting mirrors and a partially reflecting beam-splitter. The energy of each laser pulse transmitted from the beam-splitter is measured using an energy meter (ES111C, Thorlabs GmbH, Bergkirchen, Germany) and oscilloscope. The range of laser energies used in the experiments is 10–120 μJ. The laser pulse reflected from the beam-splitter is directed on to a dichroic mirror which is used to reflect the laser light to

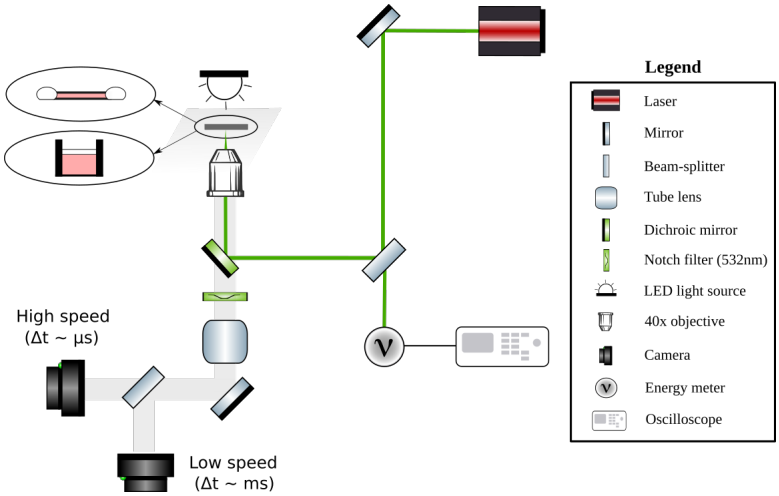

Figure 2.1: A detailed sketch of the experimental setup with the components used to produce laser-induced cavitation bubbles.

the stage where the device is placed. An inverted microscope arrangement consisting of an infinity corrected 40x objective (LUCPLFLN40X, Olympus, Tokyo, Japan) with a numerical aperture (NA) of 0.6 is aligned to focus the laser beam at a point inside the solution. A red LED light (M625L4, Thorlabs GmbH, Bergkirchen, Germany) is used to illuminate the sample. A notch filter provided beneath the dichroic mirror is used to completely block the reflected or scattered laser light and transmit the light from the LED for imaging. A tube lens is used to focus the magnified image from the objective on to the camera screen. The expansion and collapse of the bubble is captured using a high speed camera (Nova S16, Photron, Buckinghamshire, UK) operating at frame rate of 330,000 frames per second (fps) with an exposure time of 3 μs whereas the growth of crystals are recorded using a relatively low speed camera (EoSens 3CL, Mikrotron, Unterschleissheim, Germany) at 50 fps with an exposure time of 10 ms. The image of the complete working setup is provided in the Appendix A.

2.1.1. LASER

Laser is one of the most important components of the experimental setup. In this case, a Q-switched pulsed Nd:YAG laser (Nano L 50–50 PIV, Litron, Warwickshire, UK) is used to produce a collimated light at the source. For a more detailed introduction to the components and working of the laser, the reader is directed to refer the book of Koechner et al. [46]. Thus, the working principle of the laser will not be described in this report. The flash lamp and Q-switch are triggered externally using a digital delay generator with a delay of 96 μs. By this way, the laser can be operated either in pulsed mode by providing a fixed repetition rate or single pulse mode on-demand using an externally controlled button. Based on the design characteristics of the laser, the important laser beam parameters that define the current system are tabulated in Table 2.1.

Table 2.1: List of the laser beam parameters used in the current study.

Laser parameters	Variable	Formula	Values	Units
Wavelength	λ	–	532	nm
Beam diameter	d_b	–	4	mm
Pulse duration	t_p	–	4	ns
Beam waist (theoretical spot size)	w_0	$\frac{1.22\lambda}{\pi.NA}$	0.34	μm
Rayleigh length	z_R	$\frac{\pi w_0^2}{\lambda}$	0.7	μm

Since, the source beam diameter of the laser was slightly lesser than the pupil diameter of the objective (5.5 mm), all the light was able to enter the objective. Hence, a pair of concave and convex lenses was not required to change the diameter of the source beam. Since, it was not possible to measure the actual spot size of the laser beam due to the very high intensity at that point, the theoretical spot size is used for the subsequent calculations. The laser beam from the source was measured to be Gaussian. The estimation of the laser beam profile is provided in the Appendix B. The pulse-to-pulse variation in the laser energy was estimated for all the energies used in the current study and the maximum deviation was found to be well within 2%.

2.1.2. CAMERAS

In the experimental setup, two cameras were employed to image and record the events that occur within the solution after laser irradiation. The camera 1, high speed camera (Nova S16, Photron, Buckinghamshire, UK), was mainly used to capture the growth and collapse dynamics of the vapour bubble by tracking the interface of the bubble as a function of time. The camera 2, relatively low speed camera (EoSens 3CL, Mikrotron, Unterschleissheim, Germany), was used to detect the formation and position of the crystals with respect to the laser focal point in a larger field of view compared to the first camera. Since, these corresponding events occur at significantly different timescales, it was not necessary to synchronize the cameras. Hence, the first camera was triggered automatically by the trigger of laser flash lamp and a delay of 50 μs was provided using a digital delay generator which was sufficient to capture at least 5 frames before laser irradiation. On the other hand, the second camera was triggered and stopped manually just before and at least 5 seconds after shooting the laser pulse respectively. The frame rates of each camera based on the nature of experiments were chosen accordingly such that the temporal resolution of the camera was sufficient to capture the lowest relevant timescales of the system following the Nyquist sampling theorem [47]. The images of the two cameras are depicted in Figure 2.2.

A proper calibration of the cameras was necessary to account for the variations in the magnification factor from the experiments as against the theoretical value caused due to optical aberrations and various other distortions. The calibration was performed using a negative combined resolution and distortion test target (R1L1S1N, Thorlabs GmbH,

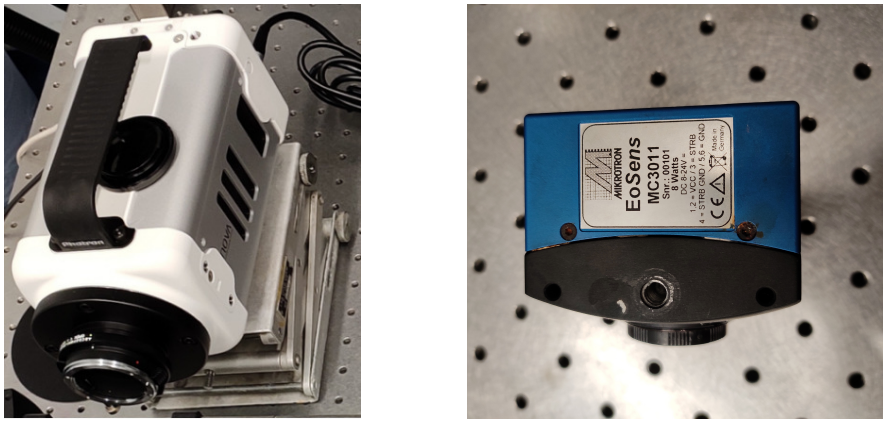

(a) (b)

Figure 2.2: a) Camera 1 (Nova S16, Photron camera) and b) Camera 2 (EoSens 3CL, Mikrotron camera).

Bergkirchen, Germany) as shown in the Figure 2.3. The test target was placed on the translation stage such that the 100 μm grid present inside it was focused sharply using both the cameras. The corresponding images of the grid were captured and the pixel values that correspond to them were measured. Using this method, the resolution of camera 1 and camera 2 were determined to be 0.5076 μm/pixel and 0.2016 μm/pixel respectively. The data acquisition and image processing for the images obtained from camera 1 and camera 2 were performed using Photron FASTCAM Viewer 4 (PFV4) and Streampix 5 software respectively. The final images recorded using the cameras were stored in the data acquisition system (or personal computer) in a raw file format or a '.tif' format so as to preserve the quality of the imaged data.

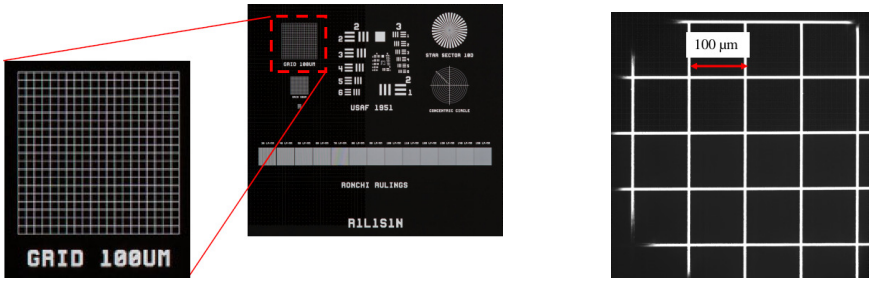

(a) (b)

Figure 2.3: a) Test target used for calibration of the camera where the inside detail depicts the 100 μm calibration grid and b) Image of the calibration grid captured using camera 1.

2.1.3. GEOMETRIES

The laser-induced cavitation experiments were performed mainly in two geometries, borosilicate glass capillaries of length 25 mm having both round and square cross-sections and cubic wells. The geometries used in the experiments are depicted in Figure 2.4.

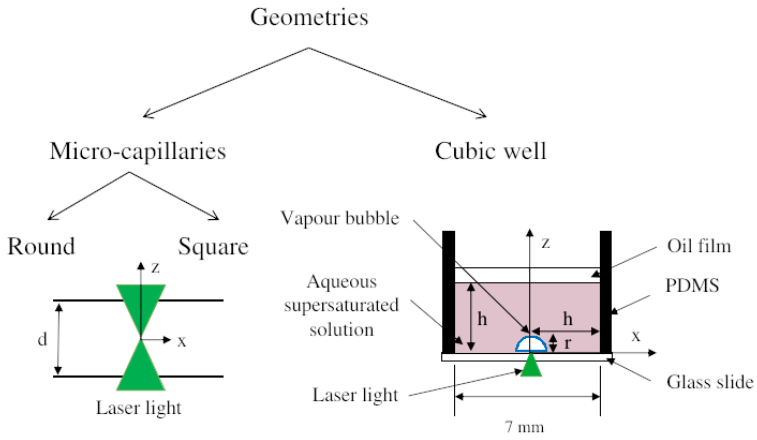

Figure 2.4: Classification of the different geometries used for performing laser-induced nucleation experiments.

The micro-capillaries (round and square, CM Scientific, Vitrocom Inc., New Jersey, USA) with internal diameters ranging from 50 μm to 300 μm were used to perform the experiments. The standard tolerances on all the capillary dimensions were within 10%. The dimensions of the micro-capillaries used in the current study are tabulated as shown in Table 2.2. During the experiments, the required solution was filled inside the capillaries by means of capillary action. The ends of the capillaries were sealed using silicone oil (kinematic viscosity, ν = 100 cSt at 25 °C, Sigma Aldrich, CAS no. 63148-62-9) in order to prevent evaporation of the solution.

Table 2.2: Details of the micro-capillaries used in the current study.

Capillary type	Inner diameter, ID (μm)	Outer diameter, OD (μm)	Wall thickness (μm)
Round	50	80	15
Round	100	170	35
Round	150	250	50
Square	50	100	25

On the other hand, cubic wells were fabricated in-house using an elastomeric material, Polydimethylsiloxane (PDMS) using a conventional molding technique. At first, a Polylactic acid (PLA) mold was printed using Fused Filament Fabrication (FFF) method in a clean environment. A mixture of PDMS base and a curing agent (Sylgard 184, Dow Europe,

Germany) in the ratio of 10:1 was poured over the mold and cured in the oven at 60°C overnight. After the sample was cured, a thin glass slide of thickness 0.13–0.16 mm was attached at the bottom of the PDMS part with the help of the above mixture and cured at 60°C for at least 2 hours. The images of the mold and final cured part are shown in Figure 2.5.

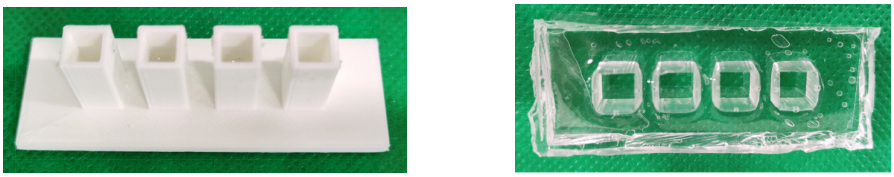

(a) (b)

Figure 2.5: a) 3D printed mold used for preparation of the device and b) Final PDMS device after curing.

In order to prevent the effect of PDMS side walls during the growth and collapse of the bubble, the distance of the wall from the centre of bubble (h) of radius r was sufficiently far such that the standoff distance, as is commonly referred in the literature, which is the ratio h/r_{max} (as denoted in Figure 2.4) was chosen to be at least greater than 10 for the largest bubble radius observed in the experiments. Similarly, the liquid height and thereby the volume of the liquid was also determined based on the same standoff distance. A thin film (~ 1.2 mm) of silicone oil (ρ = 930 kg/m^3, ν = 10 cSt at 25°C, Sigma Aldrich, CAS no. 63148-62-9) was poured over the aqueous supersaturated solution in order to prevent evaporation of the solution.

2.2. SOLUBILITY STUDIES

Solubility of the compound is one of the key parameters to be determined in a crystallization process. The procedure for determining the solubility of the sample used in the experiments are divided mainly into two parts, namely sample preparation and the overview of the equipment and operating procedures used to determine the solubility characteristics.

2.2.1. SAMPLE PREPARATION

In order to prepare the samples of the required solutions, aqueous potassium chloride (for molecular biology, ≥ 99.0%, CAS no. 7447-40-7) and a mixture of aqueous potassium chloride and potassium permanganate (ACS reagent, ≥ 99.0%, Sigma Aldrich, CAS no. 7722-64-7), for which the solubility needs to be estimated, new clean 1 ml borosilicate High Performance Liquid Chromatography (HPLC) vials were taken. The required quantity of the salt was added into the vial on a mass basis measured using a precision weighing scale (SAB225i, Adam equipment, USA) with a least count of 0.01 mg and a measurement uncertainty of ± 0.1 mg. The required amount of ultra-pure distilled water (18.2 $M\Omega.cm$, ELGA Purelab, UK) was then added to the same vial on mass basis. Magnetic stirrer was added in the vial, secured tightly with screw cap and loaded on to the crystal-16 equipment for measuring the solubility curve. The concentrations for which the solubilities have to

be determined were recorded prior to loading the samples in the equipment. The detailed protocol followed while preparing samples for the experiments are given in the Appendix C.

2.2.2. CRYSTAL-16 EQUIPMENT

The solubility measurements were performed using crystal-16 equipment (Technobis Crystallization Systems, refer Figure 2.6(a)). Crystal-16 performed integrated turbidity measurements to obtain clear and cloud points. This was done by recording the transmitted laser light via the solution to detect the presence of crystals. The solubility and metastable zone width (MSZW) of the compound was measured using clear and cloud points respectively. The clear point is the temperature at which the suspended solid material in the solution disappears. Whereas the cloud point is measured when the solid material first appears in the solution indicating the emergence of crystals.

About sixteen 1 ml vials containing solutions with different concentrations can be loaded in a single run. The steps required for the cycle of operation and input parameters such as stirring speed, heating rate, cooling rate and time taken for holding step were provided in the program accordingly. The stirring speed was kept constant at 700 rpm throughout the experiment. The steps used in determining the solubility curve for potassium chloride and potassium chloride–potassium permanganate mixture is presented in Table 2.3. Initially, a rapid heating step was provided to increase the temperature to 50°C and this temperature was held for 3 hours in the next step to ensure complete dissolution of the solute. Then, the equipment was tuned with the clear solution indicating a 100% transmission. In the next step, the solution was cooled down at a rate of 0.3°C/min to a temperature of 5°C. Following this, the solution was held at this temperature for about 3 hours to give a buffer time for spontaneous nucleation to happen in all the samples. The solution was again heated up to 50°C at a rate of 0.05°C/min and held for another 3 hours. This cycle was repeated for a total of three times to triple the data points obtained for each experiment. Figure 2.6(b) represents a cooling–heating cycle indicating the precise detection of clear and cloud points.

Table 2.3: Program used for crystal-16 experiments. Steps 3–6 are repeated thrice in total.

Step	Operation	Temperature [°C]	Time [hrs]	Rate [°C/min]
0	Ramp	50	–	10
1	Hold	50	3	–
2	Tune	–	–	–
3	Ramp	5	–	– 0.3
4	Hold	5	3	–
5	Ramp	50	–	0.05
6	Hold	50	3	–

After the program was done running, the data obtained from crystal-16 was processed using Crystal Clear software. The clear point was obtained such that the transmissivity reached the

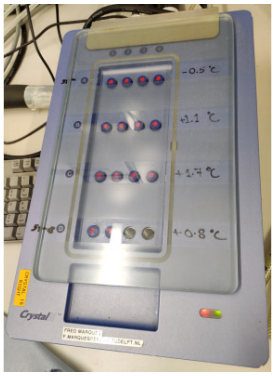

(a)

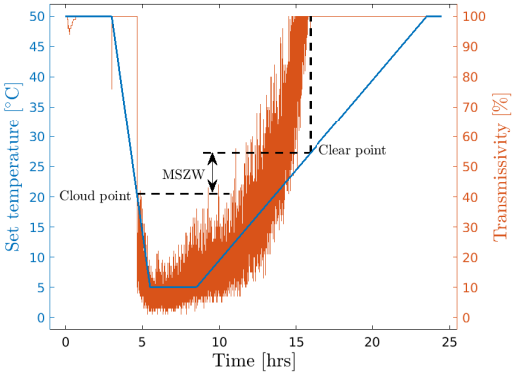

(b)

Figure 2.6: a) Crystal-16 equipment that is used to estimate the solubilities of different compounds and b) A typical example plot depicting the data obtained from crystal-16 equipment.

value of 100% and remained without changing whereas the cloud point was obtained at the point when the transmissivity suddenly dropped from 100%.

2.2.3. SOLUBILITY CURVES

The solubility curves of potassium chloride and potassium chloride–potassium permanganate mixture is shown in Figure 2.7(a). Each data point corresponds to the mean of at least two to five values obtained from experiments and the error bars represent the standard deviation. The error bars for the concentration values are omitted due to the fact that they are negligible compared to that of the temperature.

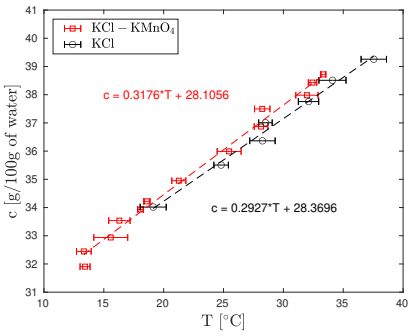

(a)

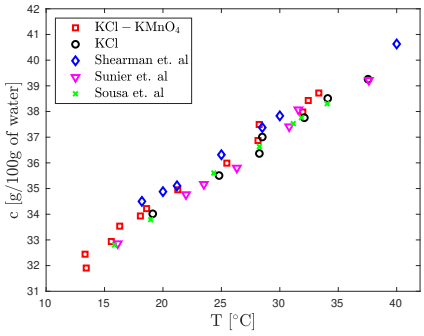

(b)

Figure 2.7: a) Comparison of the solubility curves of potassium chloride and potassium chloride–potassium permanganate mixture and b) Comparison of the experimentally obtained solubilities from crystal-16 to the existing literature data of Shearman et al. [48], Sunier et al. [49] and Sousa et al. [50].

A linear fit was constructed using least squares regression method and the equations are displayed in the plot. It can be observed from the plot that the concentrations of potassium chloride are very much comparable to that of potassium chloride–potassium permanganate mixture indicating that the addition of very small amount of potassium permanganate in potassium chloride does not affect the solubility of potassium chloride considerably. From the linear fit relation, the variation in the solubility values computed at the ambient temperature of 25°C was found to be around 1%. From Figure 2.7(b) on the right, the solubility values from crystal-16 experiments were compared with the values from literature obtained for potassium chloride in water and it can be seen that all the data overlap on to one another thereby validating the results obtained from crystal-16.

3

EXPERIMENTS IN MICRO-CAPILLARIES

> *Science never solves a problem without creating ten more.*
>
> George Bernard Shaw, *1856–1950*

In this chapter, the experiments performed with micro-capillaries and the results obtained are discussed in brief. Laser-induced cavitation has been studied inside micro-capillaries in the past with the main focus on analysing the dynamics of the bubble collapse which might aid in vigorous mixing at shorter time scales [51]. However, the main advantage lies in the fact that the geometry is essentially 1D as the bubble growth is only in the direction parallel to the axis of the capillary and the bubble dynamics are slowed down due to the presence of walls imparting a shear stress on the surface of the bubble. This allows to capture the growth and collapse of the bubble at a much lower frame rates as the total lifetime of the bubble is higher when compared to a 3D unbounded system. Sun et al. [52] developed a simple theoretical model which was sufficient to elucidate their experimental observations on the dynamics of the vapour bubble that expanded and collapsed along the axial direction of the micro-capillary. They also reported that the thermal effects played a significant role during the growth phase. Building on top of this, the key idea was to apply this existing knowledge to perform laser-induced crystallization experiments with supersaturated aqueous solutions in order to understand the mechanism of NPLIN better.

3.1. EXPERIMENTS WITH DYE

Initially, in order to benchmark the experimental setup, a mixture of water and red dye (Direct Red 81, Sigma Aldrich, CAS no. 2610-11-9) was used as it absorbs green laser light (absorption coefficient, α = 173.47 cm^{-1}, refer Appendix D) which facilitates the

formation of vapour bubble. The capillaries were filled with 0.5 wt% dye solution and the laser was focused at the centre of the capillary. The experiments were performed at ambient conditions ($T_0 \sim 25°C$). The solution was filled inside the entire volume of the tube by means of capillary action. The time evolution of the vapour bubble inside the capillary after laser irradiation is represented in Figure 3.1. It can be observed that the vapour bubble appears well within 8 μs after the point of impact of the laser and grows spherically at the start until the diameter of the capillary within the first 20 μs. After this, the bubble grows only in the axial direction due to the presence of the walls. The growth of the bubble is suppressed due to the effect of wall shear stress and the bubble reaches its maximum size at around 120 μs. After this point, the bubble starts to shrink axially as the pressure outside the bubble is greater than the pressure inside. It is important to note that the rate of expansion and collapse of the vapour bubble is much slower inside the capillary as compared to a free domain due to the effect of wall shear stress.

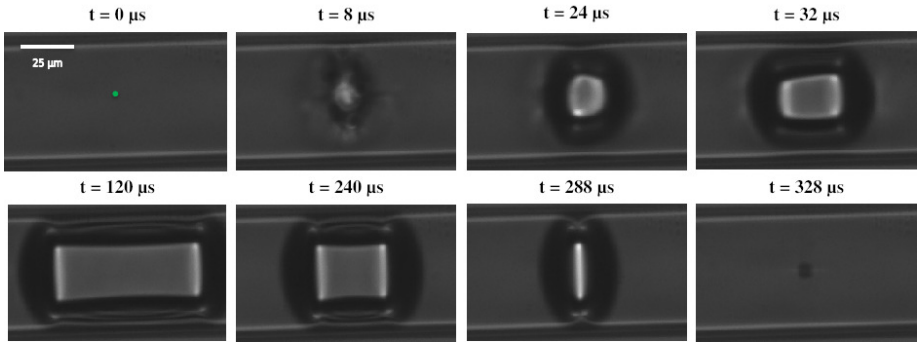

Figure 3.1: Evolution of the vapour bubble inside a round capillary with ID 50 μm and length 25 mm. The supplied and absorbed laser energies are 30.5 μJ and 20.9 μJ respectively. Images were recorded at 125,000 fps with an exposure time of 4 μs. The green point in the first image indicates the laser focal spot.

The size of the bubble varying with time was recorded from the experiments and compared with 1D numerical simulations as shown in Figure 3.2. The details of the numerical model adapted from Sun et al. [52] are given in the Appendix E. A very good agreement between the experiments and simulations can be observed indicating that a 1D model was sufficient to capture the complex flow physics inside the round capillaries. The experiments were also repeated at least three times and were found to be reproducible.

Similar experiments were performed with square capillaries (ID 50 μm and wall thickness 25 μm) in order to check the effect of curvature of the round capillaries in shifting the laser focal position and intensity at the focal spot. We observed very similar bubble dynamics as in the case of the round capillaries. However, the energy supplied to form a similar maximum bubble size was found to be much lower ($\sim$ 2.5 times) probably because the hydraulic resistance offered by the square capillary was lower ($\sim$ 0.89 times) than the circular capillary [53]. Following this, experiments were performed with supersaturated solution of potassium permanganate in water to check for the formation of crystals.

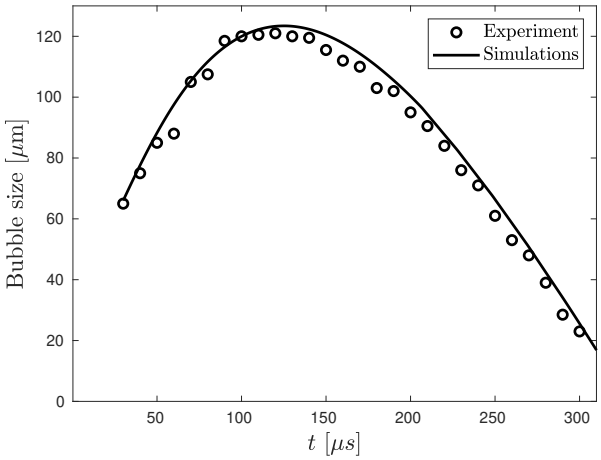

Figure 3.2: Comparison of the bubble size as a function of time between experiments and numerical simulations for a supplied laser energy of 30.5 μJ.

3.2. EXPERIMENTS WITH POTASSIUM PERMANGANATE

Potassium permanganate ($KMnO_4$) solutions in water with varying supersaturations were prepared in small 8 ml vials in order to check if it undergoes NPLIN. The solutions in the vials were maintained at 50°C for at least a day before using them for the experiments. The hot solution was filled inside the capillary and its open ends on either sides were immediately sealed using a few drops of silicone oil in order to prevent evaporation of the liquid inside the capillary. After letting some time for the solution to cool down to room temperature, the capillary was scanned to confirm the absence of crystals prior to shooting the laser. The solution was then irradiated with the laser ensuring that the surrounding glass walls were not damaged. The experimental protocol that was followed to perform these experiments is provided in the Appendix C with more details. Table 3.1 provides the observations of the experiments performed with different capillary diameters for various $KMnO_4$ supersaturations.

Experiments were performed in capillary diameters ranging from 50–150 μm, and maximum laser energies of 60 μJ, 100 μJ and 107 μJ were employed for capillary diameters of 50 μm, 100 μm and 150 μm respectively. From the observations recorded in Table 3.1, it can be noticed that none of the attempts that were carried out yielded crystals after a single shot of laser pulse. However, at a supersaturation of 1.8, crystals were observed after shooting multiple laser pulses in the 150 μm capillary. Unfortunately, these experiments were not reproducible and the crystal formation could have occurred due to some external factors which remain unknown. Furthermore, experiments were also performed in round capillaries with ID 300 μm and 70 μJ laser energy. Crystals were observed in the solution after single laser pulse for a supersaturation of 1.5. Nevertheless, the bubble formation and crystal growth could not be imaged properly due to the intense colour of the solution within the larger capillary diameters.

Table 3.1: Experimental observations of NPLIN in supersaturated aqueous potassium permanganate solution; ✓ indicates that crystals were observed after laser irradiation, ✗ indicates that crystals were not observed after laser irradiation, * indicates that crystals were observed before laser irradiation, i.e., unstable solution and ** indicates that the experiment was not reproducible.

Supersaturation (S)	**Capillary ID (μm)**		
	50	**100**	**150**
1.4	✗	✗	✗
1.5	✗	✗	✗
1.6	✗	✗	✗
1.7	✗	✗	✗
1.8	✗	✗	✓**
1.9	✗	✗	✗
2.0	✗	✗	✗
2.1	✗	✗	✗
2.2	✗	✗	✗
2.5	✗*	✗	✗

In the past, Soare et al. [54] had performed experiments with aqueous $KMnO_4$ solutions at higher ambient temperatures (T_0 = 29 °C) with the solution filled between two parallel glass plates separated by a gap of 50 μm. Crystals were observed for a laser energy of 60 μJ and for a supersaturation of 1.14. However, it is important to note that the glass around the laser focal spot was damaged upon impact of the laser in their experiments which could possibly have acted as heterogeneous sites influencing the formation of nuclei at such relatively lower supersaturations. In spite of that, these aforementioned observations from our experiments indicate that there is an effect of the geometry. In smaller capillaries, the bubble is surrounded closely by the walls on all sides which could play a role in suppressing the nucleation process possibly because of the pressure reflected by the walls of the capillary. This reflected pressure is speculated to restrict the growth rate of the vapour bubble and subsequently lower the rate of evaporation at the vapour–liquid interface which is an unfavourable condition for solute concentration accumulation at the interface. Hence, a cubic well geometry as shown in Figure 2.4 is used in the later part of this work as it offers several advantages over the capillaries as discussed in Table 3.2.

3.3. EXPERIMENTS WITH POTASSIUM CHLORIDE

In an attempt to overcome the challenges faced while handling and performing experiments with an intense colored compound such as $KMnO_4$, supersaturated aqueous potassium chloride (KCl) was used. As aqueous KCl is a colourless solution, a small amount of

undersaturated $KMnO_4$ (S = 0.1, 3.27×10^{-3} wt%) was added so as to induce colour and hence enhance the solution's absorbance to 532 nm wavelength. This idea was inspired from the work of Soare et al. [54] where laser-induced nucleation in supersaturated aqueous ammonium sulphate was performed by adding a few drops of magenta ink. The main advantages of using this KCl–$KMnO_4$ mixture for the experiments are as follows:

- *Potassium chloride:* From the previous research, KCl is well known to possess various advantages over other compounds for studying NPLIN [21]. A single nanosecond laser pulse can nucleate the solution and form visible crystals within a few seconds. Unlike urea, it does not require aging to undergo NPLIN, thereby aiding sample preparation.
- *Colour*: KCl in water is a transparent solution and does not absorb green laser light at lower energy intensities. When a small amount of $KMnO_4$ is added to aqueous KCl, it provides just enough colour to the solution which facilitates the absorption of laser light and thereby allowing to perform laser-induced cavitation experiments at lower energies than the optical breakdown threshold of water (refer Appendix F).
- *Solubility*: The addition of $KMnO_4$ to aqueous KCl solution is a case of common ion effect [55] wherein there is a possibility of decrease in the solubility of KCl as $KMnO_4$ has the same K^+ ions. Since, the quantity of $KMnO_4$ added was very low and was highly undersaturated, it was found to not affect the solubility of KCl significantly. The solubility curves of both KCl and KCl−$KMnO_4$ in water are presented in Figure 2.7(a).
- *Imaging*: As the mixture contained very small amounts of $KMnO_4$, the colour of the solution was not as intense as compared to the aqueous solutions of dye or $KMnO_4$. This allowed better contrast during imaging and reduced the effort required for post-processing in terms of quality enhancement of the recorded images from the high speed camera.

Preliminary experiments with KCl−$KMnO_4$ were performed in a 50 μm round capillary and the evolution of bubble was imaged as depicted in Figure 3.3. It can be seen that two bubbles were formed just after the laser impact and slightly higher energy was required to form a bubble than in dye due to reduced laser absorption in KCl−$KMnO_4$ solution (refer Appendix D). Although, the reason for the two or multiple bubble formation is unknown up to now, similar instances were observed when the experiments were repeated multiple times in the same capillary and even with the 50 μm square capillaries suggesting that the effect was not probably due to the geometry of the capillary. The experiments under the same conditions were also performed with ammonium chloride (NH_4Cl)–$KMnO_4$ mixture and very similar events were observed. However, this was not observed in aqueous dye solution indicating that the formation of two or multiple bubbles could be an artefact of the physical properties of the solution. As the existing 1D numerical model assumes only the formation of a single bubble, it cannot be applied for the current case.

The advantages and disadvantages of both the micro-capillary and cubic well geometries are discussed briefly in Table 3.2 as shown below.

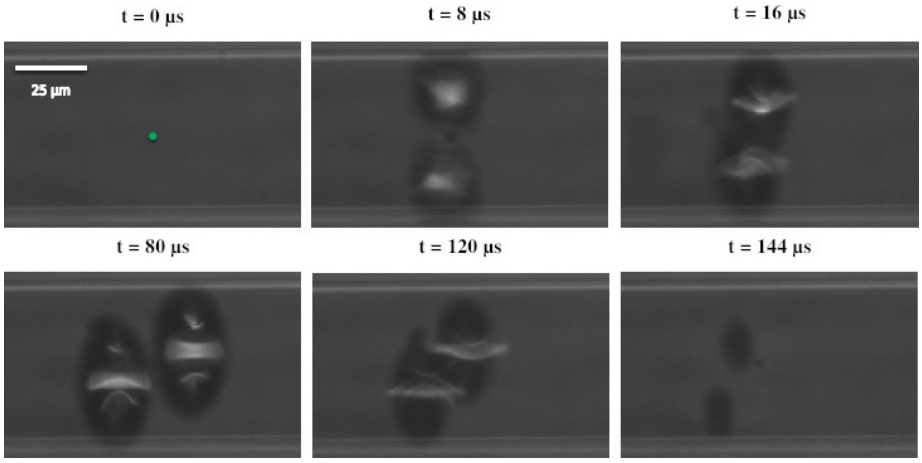

Figure 3.3: Growth and collapse of the vapour bubble in supersaturated aqueous KCl−$KMnO_4$ solution for a supplied laser energy of 57 μJ. The green point in the first image indicates the laser focal spot.

Table 3.2: Advantages and disadvantages of the different geometries used to study laser-induced cavitation.

Geometries	Positives	Negatives
Micro-capillaries	• Longer bubble lifetime, $\mathcal{O}$[100 μs] • Possible to apply 1D assumption in the simulations	• Two separate numerical models required for simulating spherical and axial bubbles respectively • Slower growth of the spherical bubble in the experiments when compared to simulations • Two bubble formation in experiments with KCl−$KMnO_4$ solutions • Difficult to handle
Cubic wells	• Possible to apply 1D assumption in the simulations • Single spherical bubble model is sufficient • Relatively easier to handle	• Shorter bubble lifetime, $\mathcal{O}$[10 μs]

4

EXPERIMENTS IN CUBIC WELLS

“ Success is a science; if you have the conditions, you get the result. ”

Oscar Wilde, *1854–1900*

In the previous chapter, the advantages of the cubic well geometry over micro-capillaries were discussed briefly. Due to the significant advantages of cubic well geometry over the micro-capillaries, further experiments were performed in cubic wells retaining all the other knowledge obtained from the experiments in the micro-capillaries.

Experiments were performed with $KCl-KMnO_4$ solutions filled in the cubic wells and the results obtained are presented in this chapter. In this system, the cavitation bubbles were created very close to the bottom wall mainly for two reasons. First, the glass slide present in the bottom side would act as a plane of symmetry for a hemispherical bubble that is expected to grow and collapse on the top side [56]. Theoretically, this allows the bubble to be considered as spherical (radially symmetric in all directions) and the governing equations pertaining to the dynamics of a spherical bubble can be applied to analyze the bubble. Secondly, crystals formed after the laser irradiation are denser than that of the liquid solution and hence they tend to settle at the bottom allowing to focus them clearly during imaging. The bubble radius $R(t)$ is considered to be the radius of the bubble image that is projected on to the camera. The impurities inherently settled near the bottom wall in the solution which are of the order of 1 μm are used to keep the focus of the laser close to the bottom wall.

4.1. CAVITATION BUBBLE DYNAMICS

4.1.1. TIME EVOLUTION OF THE BUBBLE

The radial growth and collapse of the bubble was captured by tracking the interface of the vapour bubble as a function of time using the high speed camera. The temporal evolution

of the bubble radius formed immediately after the laser impact for several laser energies is depicted in Figure 4.1(a). It can be observed that the maximum radius of the bubble increases with increase in the laser energy supplied as expected. The liquid surrounding the focal point of the laser gets superheated and the bubble expands very rapidly at the start. It is interesting to note that for all the energies the mean R at the beginning of the growth phase is very similar. It is speculated that this similarity in the trends close to the formation of the bubble are due to the bubble dynamics primarily being dictated by the pressure energy created by the laser. However, the maximum size of the bubble is expected to be governed by the thermal energy surrounding the vapour bubble, which is proportional to the supplied laser energy. It should be noted that the radius values indicated by the different markers are the mean values of at least 10 trials performed for each energy and the error bars represent the standard error of the means which is calculated as $\frac{\sigma}{\sqrt{N}}$, where σ is the standard deviation of the population and N represents the total number of trials. A typical example showing the evolution of the bubble imaged from the bottom wall to the top is shown in Figure 4.1(b). The field of view is reduced to a thin strip owing to the high frame rate (330,000 fps) employed to capture the relevant timescales of bubble dynamics. The inside of the bubble appears darker although it is transparent because the surface of the bubble acts as a diverging lens and hence the illumination light gets refracted.

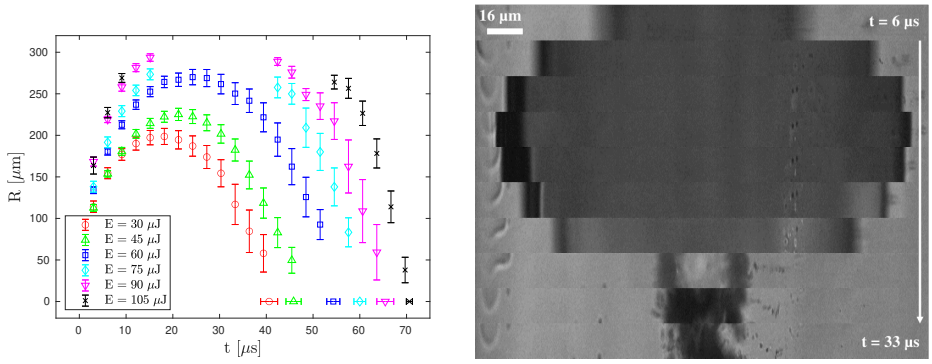

(a) (b)

Figure 4.1: a) Radial growth and collapse of the bubble for different laser energies supplied and b) An example of bubble evolution as a function of time observed using high speed camera operated at 330000 fps.

4.1.2. EXPERIMENTAL REPEATABILITY

In order to check the repeatability of the experiments performed to study the bubble dynamics, the experiments under the same conditions were repeated for five trials in supersaturated aqueous KCl−$KMnO_4$ with the supersaturation of KCl being 1.01. It is can be observed from Figure 4.2 that, for a supplied laser energy of 45 μJ, there is a significant variation in the maximum bubble radius and the collapse time for each trial with the least value of R_{max} being close to that of an average 30 μJ bubble and the other extreme being close to the average bubble size obtained for 60 μJ. This variation cannot be attributed to the difference

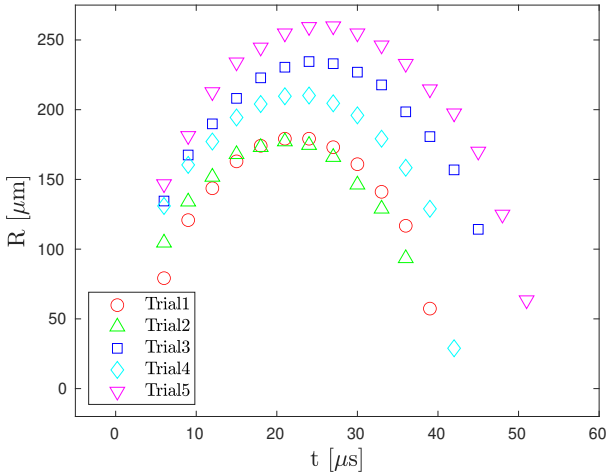

Figure 4.2: The variation in the bubble size observed for different trials in a supersaturated aqueous $KCl-KMnO_4$ solution with S = 1.01 and E = 45 μJ.

in laser energies between each trial as they were estimated to be around $\pm 0.6\,\mu$J, in this case. However, the variations are expected to arise as a result of the stochastic nature of vapour bubble creation process since a comparable margin of error in the maximum bubble radius ($\pm 37.2\%$) was documented in the similar experiments performed by Quinto-Su et al. [57].

4.1.3. COLLAPSE TIMESCALES

From the radius–time plots, it is evident that the observed time of growth of the bubble is very close to it's collapse time (time taken for R to go from maximum to zero). The total lifetime of the bubble (also commonly referred to as the oscillation time) obtained from the experiments is in agreement with the analytical prediction indicating that the hemispherical bubble created behaves like a sphere [58]. In this case, the generalized Rayleigh–Plesset equation is used to describe the dynamics of the bubble. In order to analytically estimate the collapse time of the bubble, the viscous effects, surface tension effects and the effects of non-condensable gas can be neglected based on an order of magnitude analysis considering the larger size of the bubble formed and the resulting governing equation reduces to the well known Rayleigh equation [59] given by

$$R\frac{d^2R}{dt^2} + \frac{3}{2}\left(\frac{dR}{dt}\right)^2 = \frac{p}{\rho} \tag{4.1}$$

where R is the radius of the bubble, p is the pressure far away from the bubble and ρ is the density of the solution. Based on the above equation, the Rayleigh collapse time can be derived as follows.

$$T_c = 0.915 R_{\max}\left(\frac{\rho}{p}\right)^{0.5} \tag{4.2}$$

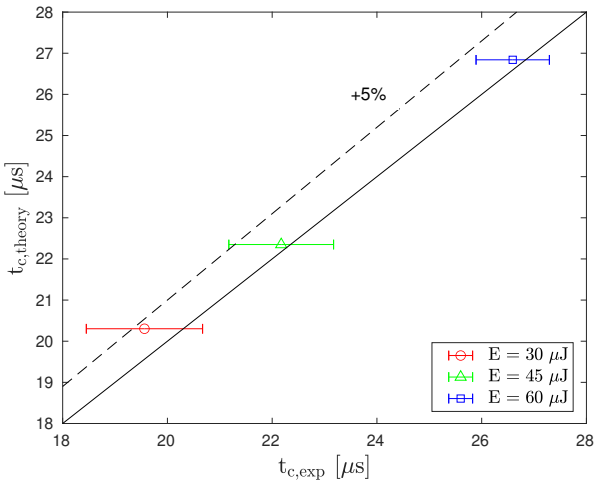

Figure 4.3: Comparison of theoretical and experimental collapse times of the bubble for different laser energies supplied.

The theoretical collapse time estimated using the above equation is compared with the experimentally obtained collapse time in order to validate the experimental results as portrayed in Figure 4.3. It can be seen that the experimentally obtained collapse times of the bubble compare reasonably well with the theoretically estimated values with the maximum deviation being within 4% in the observed range of energies. The relatively larger deviation for 30μJ as compared to the other higher energies could be attributed to the fact that the maximum bubble radius becomes relatively smaller as the energy reduces and this brings into play the effects of viscosity and surface tension which were mainly neglected due to the larger bubble sizes. Adding to this, the number of trials performed for the energy of 30 μJ (N = 10) is lesser than that of the other two energies (N = 15) which might also play a role in terms of lower statistical numbers. For energies greater than 60 μJ, it was not possible to experimentally obtain the maximum bubble radius as the bubble happened to be larger than the maximum field of view affordable using the high speed camera in the current setup.

4.1.4. RELATION BETWEEN LASER ENERGY AND BUBBLE RADIUS

From the experiments, the parameters that are systematically varied between each experiment are the laser energy and solution supersaturation. Correspondingly, the observed outputs are the bubble size and the position or number of crystals formed. From Figure 4.1, it can be observed that the maximum radius of the bubble increases as the energy supplied by the laser increases. However, it can be noticed from the same plot that the relation is not exactly linear as then we would have obtained a linear increase in the collapse times. Hence, it would be useful to estimate the relationship between the laser energy supplied and maximum size of the bubble as such a relation would be very convenient in predicting the maximum radius apriori while knowing the laser energy. Hence, the maximum bubble radius for laser energies up to 75 μJ obtained from the experiments were plotted in order to check if there were any

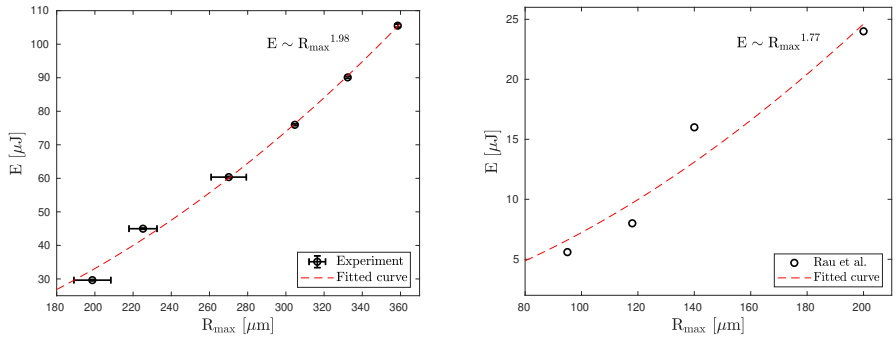

Figure 4.4: a) Relation between the supplied laser energy and maximum bubble radius from the experiments performed in this work and b) Variation of the maximum radius as a function of the laser energy obtained from Rau et al. [60].

observable trends. Since, the theoretical collapse times matched closely with the experiments for laser energies up to 60 μJ, the maximum radius was therefore estimated theoretically based on the experimentally obtained oscillation times (t_{osc}) for higher energies. Assuming that $t_{osc} = 2t_c$, the theoretically computed $R_{\max}$ values were plotted against the supplied laser energy as shown in Figure 4.4(a). It can be inferred from the plot that the laser energy varies proportionally with the square of the maximum radius. In order to further verify this observed relation between laser energy and $R_{\max}$, the experiments performed by Rau et al. [60] on epithelial cells in polystyrene culture dishes were analyzed where the maximum radius was measured for different laser energies supplied. A qualitative agreement in the trend was obtained while comparing them with our experiments, although, the power law fit, in their case, yielded a slightly lower value when compared to our case as shown in Figure 4.4(b).

4.2. ASPECTS OF CRYSTALLIZATION

Having looked at some facets of the bubble dynamics to get some insights into the growth and collapse of the vapour bubble, both the KCl supersaturation and the laser energy were systematically varied until the occurrence of crystals. This systematic analysis also allowed us to determine the approximate energy threshold for each supersaturation at which crystals were observed. Following this, some of the parameters such as the nucleation probability and number of crystals were calculated to check if there are any significant trends that can be noticed.

4.2.1. EFFECT OF LASER ENERGY AND SUPERSATURATION ON THE NUCLEATION PROBABILITY

By varying the supersaturation of KCl and the supplied laser energy, a phase map for nucleation probability was generated based on the occurrence of crystals. The nucleation

probability, in this case, is defined as the number of trials in which crystals were observed to the total number of trials performed. For all the energy–supersaturation combinations, at least 5 trials were performed to estimate the nucleation probability. From the Figures 4.5(a) and 4.5(b), the following observations are made:

- For a fixed supersaturation, as the energy increases the nucleation probability also increases but not in a linear manner.
- Similarly, for a fixed laser energy, as the initial supersaturation of the solution increases, there is a non-linear increase in the nucleation probability.
- The increase in the nucleation probability with respect to increase in the laser energy was observed to be more gradual for higher supersaturation. Whereas, for lower supersaturations, this change in nucleation probability was found to be more sharper.

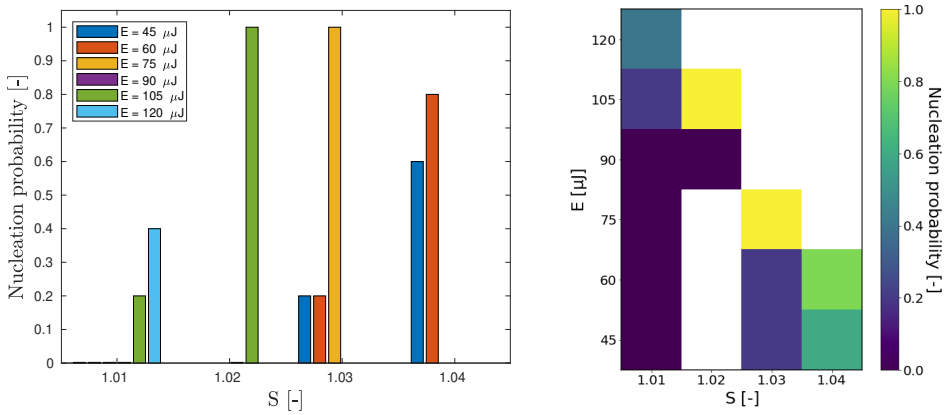

(a) (b)

Figure 4.5: a) Variation in the nucleation probabilities as a function of solution supersaturation and laser energy supplied and b) Colour map representing the energy threshold for crystal formation for different supersaturations of aqueous KCl. White regions in the color map indicate that the experiments were not performed in that regime.

4.2.2. NUMBER OF CRYSTALS

In addition to checking both the formation and the location of the crystals formed, the number of crystals for each set of laser energy and solution supersaturation were also quantified. For a given supersaturation, it was observed that, as the laser energy increases the crystal count also increased above a certain energy threshold. Similarly, for a given laser energy, as the supersaturation of the solution was increased, an increase in the nucleation probability was observed. This observation is expected as an increase in the solute concentration or supersaturation at the vapour–liquid interface would lead to an increase in the crystal nucleation rate (number of nuclei per unit volume per unit time). These above mentioned observations are represented in Figure 4.6(a).

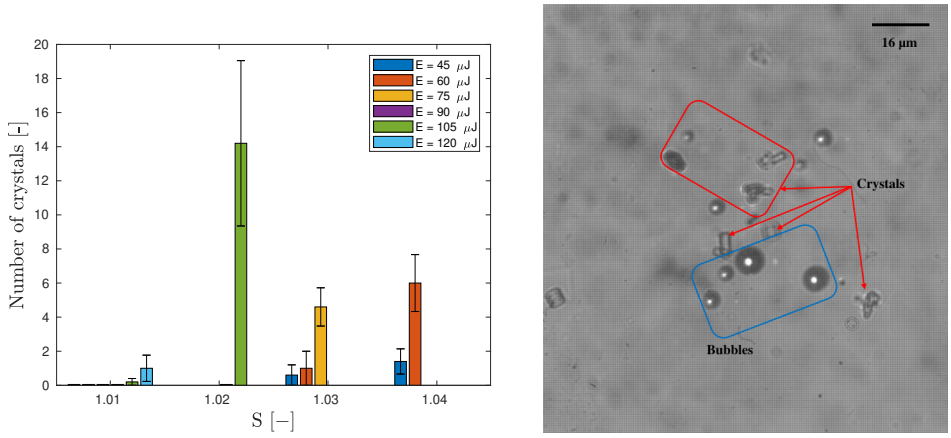

(a) (b)

Figure 4.6: a) Number of crystals observed as a function of solution supersaturation and laser energy supplied and b) A typical example of crystal formation as observed using the camera 2. Image represents a supersaturated aqueous KCl–$KMnO_4$ solution with S = 1.02 and E = 105 μJ at $t = 5\,s$ after laser irradiation.

4.2.3. GENERAL OBSERVATIONS

Some of the general observations that were encountered while performing the laser-induced cavitation experiments are listed below.

1. From the experiments performed, the shape of the crystals formed can be classified mainly into three types as illustrated in Figure 4.7:
   - *Planar:* These are rectangular crystals that grew into a large size while the growth was relatively larger on one set of parallel sides compared to the other.
   - *Cube:* These crystals grew in to a medium size with uniform growth on all the sides.
   - *Needle-like*: These crystals grew into a large size while the growth was only along one particular direction.
2. The farthest position at which crystals were identified was found to be roughly 0–3 times the maximum bubble radius from the point of laser focus in all the experiments. This can probably be attributed to the jet created each time during the collapse of the vapour bubble that could possibly advect away the nuclei formed before it grows into a significant size. The direction of the jet formed after bubble collapse was found to be random. One such example of the jet is shown in Figure 4.8.
3. For the instances where the bottom glass was accidentally damaged by laser, we observed the formation of crystals even for lower energy (30 μJ) and lower supersaturation (S = 1.03) than that of the threshold. In addition, the number of crystals formed were found to be comparatively high (>10 crystals) as shown in Figure 4.9.

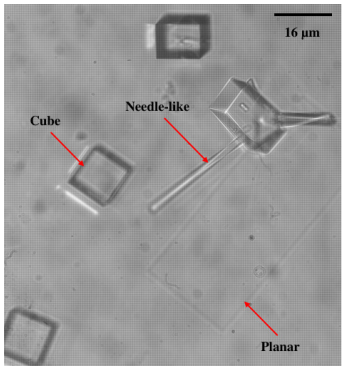

Figure 4.7: Formation of different crystal shapes in aqueous KCl–$KMnO_4$ solution with S = 1.03 and E = 75μJ.

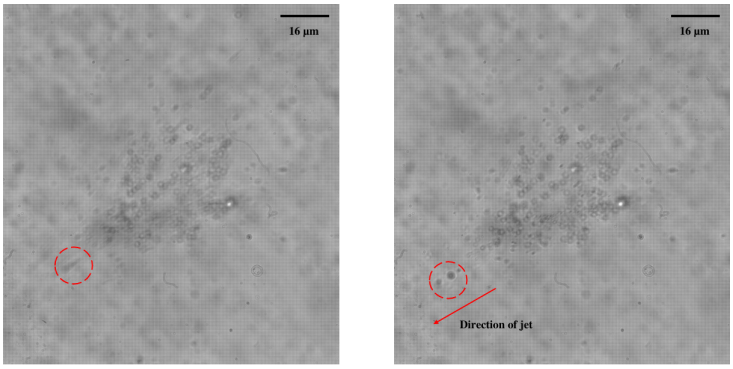

(a) (b)

Figure 4.8: The direction of the jet created due to the collapse of the vapour bubble. Image taken at: a) 20 ms and b) 40 ms after laser irradiation respectively. A few residual bubbles are circled with a red dashed line to show its motion in the subsequent frame.

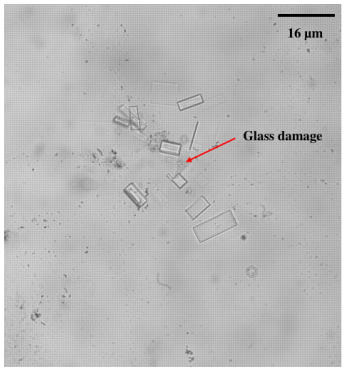

Figure 4.9: Formation of crystals surrounding the glass damage due to laser in aqueous KCl–$KMnO_4$ solution with S = 1.03 and E = 30μJ.

5

CONCLUSIONS AND RECOMMENDATIONS

> *If you can't explain it simply, you don't understand it well enough.*
>
> Albert Einstein, *1879–1955*

This chapter provides some final insights on this thesis by first summarising the work done and then drawing appropriate conclusions to support the evidence. The conclusions are then followed by recommendations that would serve to be useful for future work and provide scope for further improvements.

5.1. SUMMARY

- An experimental setup was designed, developed and tested to study the effects of laser-induced cavitation in supersaturated aqueous solutions.
- Experiments were performed both in confined and unconfined geometries, and the influence of each system on the laser-induced vapour bubble dynamics and crystal formation were studied.
- In the employed experimental technique for the unconfined geometry, the dynamics of the hemispherical vapour bubble's growth and collapse were analyzed so as to benchmark it against a free unbound spherical bubble – a phenomena that is speculated to happen in NPLIN experiments.
- For the unconfined geometry, the effect of the laser energy and supersaturation of aqueous potassium chloride on the nucleation probabilities were analysed. The range of laser energy thresholds for which crystals starts to occur in various supersaturations were determined.

5.2. CONCLUSIONS

- The growth and collapse of the vapour bubble for different laser energies in an unconfined geometry was quantified from the experiments. It was observed that the mean radius at the start of each bubble's expansion was identical, and a symmetry in the radius–time profile was observed although the governing process during the growth and the collapse phases differ.
- For the vapour bubbles created, the theoretical collapse times were very similar to the collapse times observed in the experiments with a maximum deviation of 4%.
- The laser energy supplied to the solution was found to scale with the square of the vapour bubble's maximum radius.
- For the system containing supersaturated potassium chloride, a phase map of nucleation probability for different values of laser energies and supersaturation was obtained. A minimum threshold energy was observed to be required for the formation of crystals. This threshold energy was found to be lowered with an increase in the supersaturation of the solution.
- Furthermore, for the experiments using supersaturated aqueous potassium chloride, the number of crystals formed for different laser energy–supersaturation combinations were recorded. Beyond the threshold laser energy for crystallization, this crystal number was found to increase with the laser energy.

5.3. RECOMMENDATIONS

- As nucleation is regarded to be a stochastic process, experiments should involve considerable number of repetitions in order to be statistically significant. In the current study, only five trials were performed for each experiments that were involved in determining the crystal nucleation probability. Hence, it is advised to perform more trials in order to improve the accuracy of the outcomes.
- In the present study, the supersaturation of potassium chloride was limited to 1.04 due to the reason that the solution nucleated more often even before laser irradiation. Either by improving the hydrophobization technique or by choosing an alternate material for device construction, higher supersaturations such as 1.05 and 1.06 could be achieved to extend the phase map further.
- With the experimental results from the current work, a simple numerical model can be developed to analyze the solute mass transfer surrounding the vapour bubble leading to the crystal formation.
- With the recorded crystal growth rate using the low speed camera, the kinetics of crystal growth can be studied. This might provide more insights into the process which can then be extended or compared to the larger systems such as millimeter-sized vials and industrial crystallizers.

A

EXPERIMENTAL SETUP

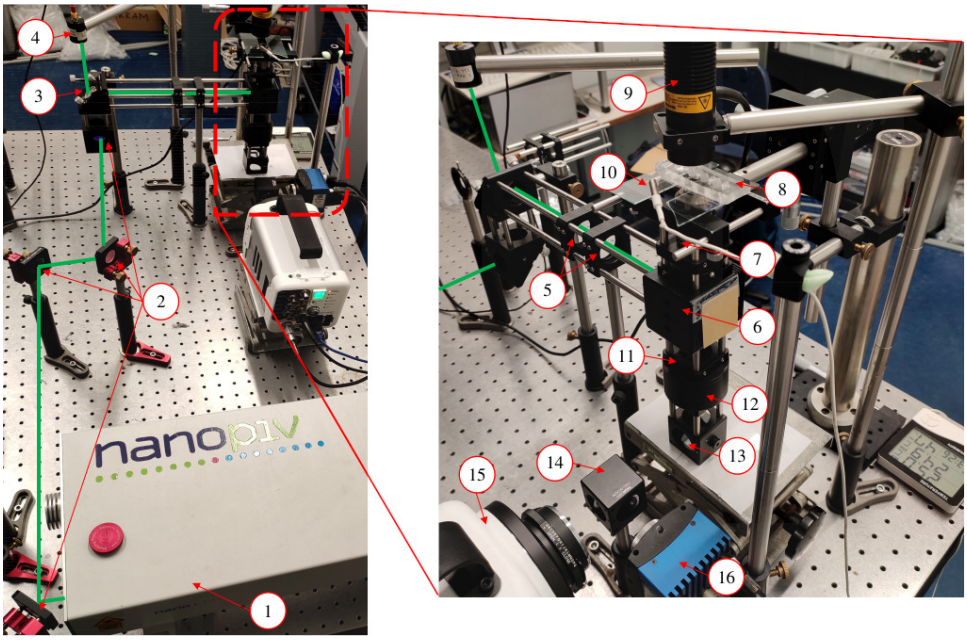

Figure A.1: Layout of the experimental setup with the components annotated as, 1) Laser, 2) & 13) Fully reflecting mirrors, 3) & 14) Beam-splitters, 4) Energy meter, 5) Concave and convex lenses, 6) Dichroic mirror, 7) 40x objective, 8) Manual translation stage, 9) Red LED light, 10) Temperature probe, 11) Notch filter, 12) Tube lens, 15) High speed camera and 16) Low speed camera.

B

LASER BEAM PROFILE

The estimation of the beam profile was done by measuring the average energy of the laser by blocking the beam diameter in steps of 0.5 mm. A normalized value (with respect to the predicted peak laser intensity) of the measured profile is shown in Figure B.1. The corresponding intensity (in MW/cm^2) as a function of beam's radial position was calculated using the energy measured and the area of the incident circular laser beam. The Gaussian fit is given by

$$I_{\text{norm}} = A \exp - \left\{ \left(\frac{r - B}{C} \right)^2 \right\} \tag{B.1}$$

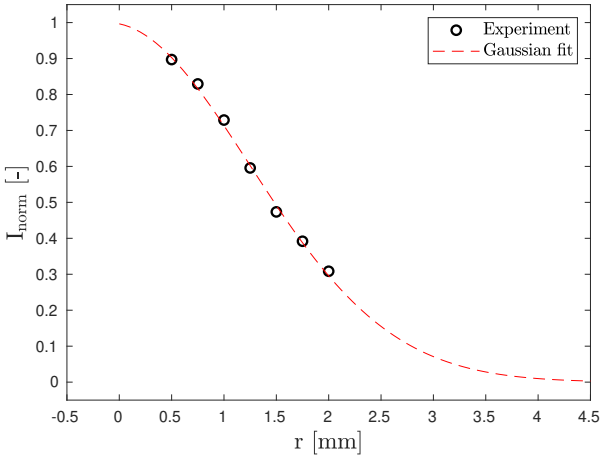

Figure B.1: Measured variation in the laser intensities as a function of beam's radial position.

where I_{norm} is the normalized laser power intensity, r is the radial position from the axis of the laser beam, the constants A, B and C indicate the highest intensity, radius at which the

intensity is the highest and the standard deviation corresponding to a confidence interval of 95% respectively. From the above plot, it can be observed that the experimentally determined intensities follows the Gaussian distribution which indicates that the beam profile is near-Gaussian.

C

EXPERIMENTAL PROTOCOLS

C.1. SAMPLE PREPARATION

- Place a filter paper over the petridish and fill some potassium chloride over it. Once it is done, immediately close the container to avoid contamination
- Take a clean 8 ml HPLC vial and keep it on a weighing scale and tare it to zero. Add the required amount of potassium chloride to the vial from the petridish

  The amount of solute required to obtain the desired supersaturation can be calculated for 7 ml of water as amount of solute (g) = solubility at 25°C (g/100g of water) * degree of supersaturation / 7
- Discard the excess potassium chloride properly
- Pipette out 7 ml of water to add to the vial and record the weight of water added
- Add a magnetic stirrer and place it in a hot plate at 25°C, 1500 rpm and wait for a few minutes until the salt dissolves
- Place the vial inside the oven maintained at 50°C at least overnight in order to dissolve the remaining salt

C.2. MICRO-CAPILLARY EXPERIMENTS

- Remove the vial containing the solution from the oven maintained at 50°C
- Before it starts to cool, fill the capillary with the warm solution by means of capillary action and place it on a Teflon-coated glass slide
- Seal the ends of the capillary immediately using silicone oil (ν = 100 cSt at 25°C) before the solution inside starts to evaporate

- If required, place the glass slide on a hot plate at 50°C to re-dissolve the crystals that might be formed at the ends of the capillary within this time
- Before shooting laser, ensure that there are no crystals present inside the capillary by scanning it completely using the camera
- Shoot the laser pulse, record the laser energy and room temperature and save the recorded images
- After shooting the laser, scan the capillary completely to check for the formation of crystals and damage over the capillary walls due to laser (if any)

C.3. CUBIC WELL EXPERIMENTS

C.3.1. PDMS PREPARATION

- Prepare the required amount of the PDMS mixture (PDMS base : curing agent = 10:1) in a centrifuge tube
- Mix well with spatula until it turns opaque due to air bubbles
- Centrifuge the mixture at 7400 rpm for 15 minutes to get rid of the impurities
- Pour the mixture around the 3D printed mold placed inside a petridish
- Place the petridish in a vacuum chamber for 5 minutes to get rid of air bubbles
- Transfer the sample to the oven at 60°C for at least 12 hours
- Ensure that the PDMS is cured properly and then cut the required portion of the cured PDMS
- Apply the PDMS mixture on the bottom surface of the cured PDMS and attach a clean glass slide to it
- Cure it in the oven at 60°C for at least 4 hours and ensure if the glass slide is attached firmly to the PDMS

C.3.2. HYDROPHOBIZATION OF DEVICE

- Remove any dirt in the PDMS device using compressed air
- Pipette 10μL of trichloro(1H,1H,2H,2H-perfluoroctyl)-silane into a clean petridish
- Place both the PDMS device and petridish in a vacuum chamber for at least 2 hours
- After 2 hours, remove the PDMS device and check if the coating is applied. If not, keep it back for another 1 hour

C.3.3. BEFORE SHOOTING LASER

- Remove the vial from the oven and place it in the hot plate at 50°C
- After 1 minute, turn on stirrer at 1000 rpm for approximately 1 minute and turn it off
- After 1 minute, fill the supersaturated solution (200μL) in a cubic well and then fill the silicone oil (10 cSt at 25°C, 60μL) on top of the solution. Place the device on the stage and allow it to cool down for approximately 7 minutes
- After 7 minutes, scan the well completely using the camera (total scanning time is around 5 minutes) in order check if there are crystals formed prior to shooting laser. If crystals are not present, proceed to the next step or else discard the sample and repeat the same procedure up to this point
- Position the well such that the laser focal spot is approximately equidistant from the side walls and within 10 μm above the bottom glass slide. The impurities sedimented on the bottom surface can be used to position the laser focus at the required distance from the bottom glass slide.
- Shoot the laser pulse

C.3.4. AFTER SHOOTING LASER

- Record the energy of the laser pulse, note down the room temperature and save the recorded images of the camera
- After around 1 minute from shooting the laser pulse, scan the well near the region of laser focus (2–3 camera frames on all sides while keeping the field of view as large as possible) to check for crystals and note down the observation
- Then scan the well completely in order to check for crystals anywhere else within the solution
- Note down both the number of crystals formed and the position of the farthest crystal from the laser focal spot
- Irrespective of whether the crystal(s) was formed or not, discard the solution and clean the well both with water and methanol
- Repeat the steps in C.3.2 before using the same well for further experiments

D

ABSORBANCE MEASUREMENTS

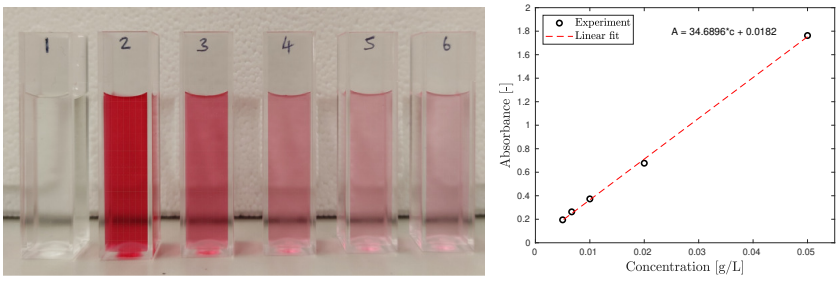

(a) (b)

Figure D.1: a) Images representing the different concentrations of dye in a glass curvette with a path length of 10 mm and b) Variation in the absorbance values for various concentrations of dye following a linear relation.

Experiments using UV-visible spectrophotometer were performed to obtain the absorbance of the solutions used. The recorded values of aqueous red dye for various concentrations are reported in the Figure D.1, where the absorbance (A) is measured using the relation

$$A = -\log_{10}\left(\frac{\phi_e^t}{\phi_e^i}\right) \tag{D.1}$$

for ϕ_e^t and ϕ_e^i are the transmitted and incident light fluxes respectively. Furthermore, to estimate the absorption coefficients of the dye concentration used in the microfluidic experiments, the relationship between the absorbance and the concentration was derived from the Beer–Lambert's law

$$A = \epsilon c l \tag{D.2}$$

where ϵ is the molar absorption coefficient, c the molar concentration and l the optical path length. Thus, for the high concentrations of red dye (5 g/L) used, the absorption coefficient was calculated by using the linear relation between absorbance and solute concentration (also achieved by extrapolating the values from Figure D.1(b). The calculated value is reported in the Table D.1.

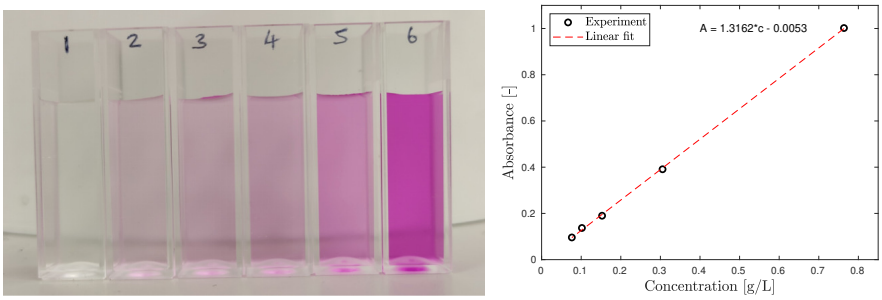

(a) (b)

Figure D.2: a) Images representing the different concentrations of $KMnO_4$ in a glass curvette with a path length of 10 mm and b) Variation in the absorbance values for various concentrations of $KMnO_4$ following a linear relation.

Similarly, the absorption coefficient for $KMnO_4$ alone was determined using the linear relation between absorbance and solute concentration (also obtained by extrapolating the values from the Figure D.2(b) and reported in the table D.1.

Additionally, it was observed that at least for 532 nm wavelength there were no differences in absorbance between air, ultra-pure water (18.2 $M\Omega.cm$, ELGA Purelab, UK) and KCl (S = 0.9). For the experiments with aqueous KCl–$KMnO_4$ solutions, a KCl supersaturation of 0.9 was used as to avoid the crystal formation during absorbance measurements. The measured absorbance in all the cases were done with respect to ultra-pure water.

Table D.1: The absorption coefficients of different compounds that were used in this study.

Compounds	**Concentration (g/L)**	**Absorption coefficient, α (cm^{-1})**
Red dye	5	173.47
$KMnO_4$ (S = 0.1)	76.363	100.504
KCl−$KMnO_4$	323.524	0.357

E

NUMERICAL MODEL

The approximate one-dimensional nature of the bubble expansion and collapse inside micro-capillaries suggests the possibility of using a simple one-dimensional numerical model for analyzing the flow dynamics. Through equation-based modelling, the COMSOL Multi-physics software (version 5.6) was used to solve the below mentioned governing equations using Finite Element Method (FEM) in order to predict the size of the axial bubble as a function of time.

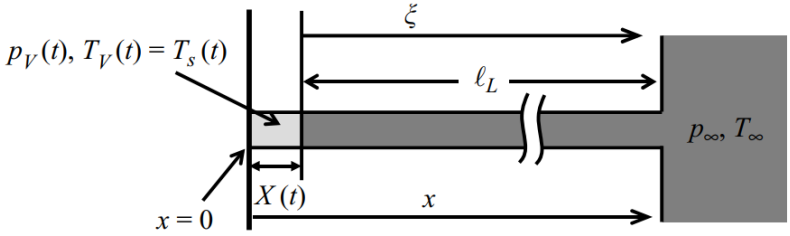

Figure E.1: Conceptual sketch used in the formulation of the 1D numerical model. Image reproduced from Sun et al. [52].

The domain considered for numerical modelling is shown in Figure E.1. The vapour is approximated to be a lumped system which is assumed to be saturated at all times with saturation pressure and temperature as p_V and T_s respectively. The pressure and temperature at the other end of the liquid column is considered to be constant as p_∞ and T_∞ respectively. The equation of motion of the liquid column in the tube can be approximated as

$$l_L \rho_L \frac{d^2X}{dt^2} = p_V(t) - p_\infty - \mathscr{R}\frac{dX}{dt} \tag{E.1}$$

where, l_L is the length of the liquid column, which is kept constant and equal to half of the tube length given the miniature size of the the bubble, ρ_L is the liquid density, p_V is the vapour pressure inside the bubble and $\mathscr{R}$ represents the approximate effect of viscous

losses due to the presence of surrounding wall. By approximating the flow in the tube as a quasi-steady, fully developed Poiseuille flow, we equate the term $\mathscr{R} = 32\mu\, l_\mathrm{L}/d^2$, where μ is the liquid dynamic viscosity.

We write an energy balance for the vapour in the following form

$$H_\mathrm{latent}\,\frac{d}{dt}(\rho_\mathrm{V} X) = k\,\frac{\partial T}{\partial x}\bigg|_{x=X} - \rho_\mathrm{V}\, c_\mathrm{s}\, X\,\frac{dT_\mathrm{s}}{dt} \tag{E.2}$$

The left-hand side of this equation is the latent heat associated with the vapour generation or condensation. The first term on the right-hand side is the energy conducted to the vapour from the liquid column where k is the thermal conductivity of the liquid. The final term is the temperature at the liquid surface accounting for the energy necessary to maintain the vapour at saturation conditions, where c_s is the specific heat along the saturation curve and $T_\mathrm{s}(t) = T(X(t), t)$.

The temperature change of the liquid column is controlled by the diffusion equation defined in the frame of reference of the moving liquid.

$$\rho_\mathrm{L}\, c_p\,\frac{\partial T}{\partial t} = k\,\frac{\partial^2 T}{\partial \xi^2}, \tag{E.3}$$

where,

$$T(\xi = 0,\, t) = T_\mathrm{s}(t), \quad T(\xi = l_\mathrm{L},\, t) = T_\infty.$$

F

PROBABILITY OF VAPOUR BUBBLE FORMATION

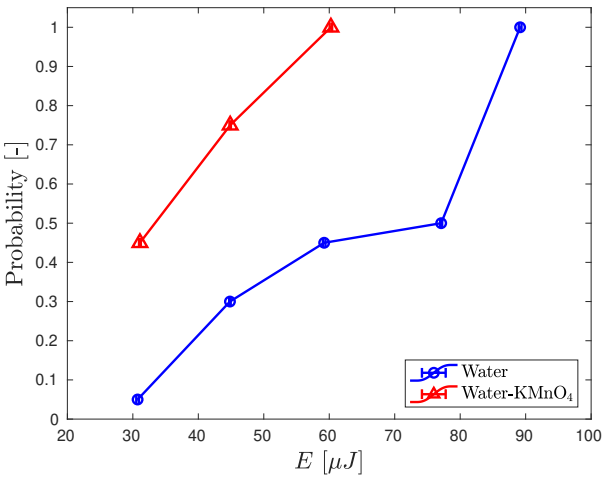

Figure F.1: Observed laser-induced cavitation probabilities for solutions of water and water–$KMnO_4$ mixture.

From the above plot, it can be seen that introducing a small amount of $KMnO_4$ (3.27×10^{-3} wt%) to ultra-pure water (18.2 $M\Omega.cm$, ELGA Purelab, UK) does increase the probability of bubble nucleation under laser irradiation. This observation is expected since the purple colour introduced by $KMnO_4$ enhances the solution's absorbance to 532 nm laser wavelength. The absorbance of the solutions have been measured and reported in Appendix D.

BIBLIOGRAPHY

[1] John William Mullin. *Crystallization*. Elsevier, 2001.

[2] Wolfgang Beckmann. *Crystallization: Basic concepts and industrial applications*. John Wiley & Sons, 2013.

[3] Alison Lewis et al. *Industrial crystallization: fundamentals and applications*. Cambridge University Press, 2015.

[4] Martin Robert Ward. "Non-photochemical laser-induced nucleation (NPLIN): An experimental investigation of crystal nucleation". PhD thesis. The University of Edinburgh, 2014.

[5] Deniz Erdemir, Alfred Y Lee, and Allan S Myerson. "Nucleation of crystals from solution: classical and two-step models". In: *Accounts of chemical research* 42.5 (2009), pp. 621–629.

[6] SW Young. "MECHANICAL STIMULUS TO CRYSTALLIZATION IN SUPERCOOLED LIQUIDS." In: *Journal of the American Chemical Society* 33.2 (1911), pp. 148–162.

[7] GR Edwards, LF Evans, and SD Hamann. "Nucleation of ice by mechanical shock". In: *Nature* 223.5204 (1969), pp. 390–391.

[8] JW Mullin and KD Raven. "Nucleation in agitated solutions". In: *Nature* 190.4772 (1961), pp. 251–251.

[9] JW Mullin and KD Raven. "Influence of mechanical agitation on the nucleation of some aqueous salt solutions". In: *Nature* 195.4836 (1962), pp. 35–38.

[10] Jin Liu and Åke C Rasmuson. "Influence of agitation and fluid shear on primary nucleation in solution". In: *Crystal growth & design* 13.10 (2013), pp. 4385–4394.

[11] Jin Liu, Michael Svard, and Åke C Rasmuson. "Influence of agitation on primary nucleation in stirred tank crystallizers". In: *Crystal Growth & Design* 15.9 (2015), pp. 4177–4184.

[12] K Visuri et al. "A new method for protein crystallization using high pressure". In: *Bio/technology* 8.6 (1990), pp. 547–549.

[13] M Taleb et al. "Crystallization of proteins under an external electric field". In: *Journal of Crystal Growth* 200.3-4 (1999), pp. 575–582.

[14] Lee Fiona Alexander and Norbert Radacsi. "Application of electric fields for controlling crystallization". In: *CrystEngComm* 21.34 (2019), pp. 5014–5031.

[15] Stanley L Hem. "The effect of ultrasonic vibrations on crystallization processes". In: *Ultrasonics* 5.4 (1967), pp. 202–207.

[16] RC Silva et al. “Effects of high intensity ultrasound frequency and high-speed agitation on fat crystallization”. In: *Journal of the American Oil Chemists' Society* 94.8 (2017), pp. 1063–1076.

[17] BA Garetz et al. “Nonphotochemical, polarization-dependent, laser-induced nucleation in supersaturated aqueous urea solutions”. In: *Physical review letters* 77.16 (1996), p. 3475.

[18] Marco Nardone and Victor G Karpov. “A phenomenological theory of nonphotochemical laser induced nucleation”. In: *Physical Chemistry Chemical Physics* 14.39 (2012), pp. 13601–13611.

[19] Andrew J Alexander and Philip J Camp. “Non-photochemical laser-induced nucleation”. In: *The Journal of chemical physics* 150.4 (2019), p. 040901.

[20] *Taming crystallization with light: nonphotochemical laser induced nucleation*. Available at https://www.tudelft.nl/3me/over/afdelingen/process-energy/research/complex-fluid-processing/running-projects/taming-crystallization-with-light-nonphotochemical-laser-induced-nucleation (2005/06/12).

[21] Martin R Ward and Andrew J Alexander. “Nonphotochemical laser-induced nucleation of potassium halides: Effects of wavelength and temperature”. In: *Crystal growth & design* 12.9 (2012), pp. 4554–4561.

[22] Julien Zaccaro et al. “Nonphotochemical, laser-induced nucleation of supersaturated aqueous glycine produces unexpected γ-polymorph”. In: *Crystal Growth & Design* 1.1 (2001), pp. 5–8.

[23] Xiaoying Sun, Bruce A Garetz, and Allan S Myerson. “Polarization switching of crystal structure in the nonphotochemical laser-induced nucleation of supersaturated aqueous l-histidine”. In: *Crystal Growth and Design* 8.5 (2008), pp. 1720–1722.

[24] Wenjing Li et al. “Non-photochemical laser-induced nucleation of sulfathiazole in a water/ethanol mixture”. In: *Crystal Growth & Design* 16.5 (2016), pp. 2514–2526.

[25] Aziza Ikni et al. “Experimental demonstration of the carbamazepine crystallization from non-photochemical laser-induced nucleation in acetonitrile and methanol”. In: *Crystal growth & design* 14.7 (2014), pp. 3286–3299.

[26] Martin R Ward, Stephanie McHugh, and Andrew J Alexander. “Non-photochemical laser-induced nucleation of supercooled glacial acetic acid”. In: *Physical Chemistry Chemical Physics* 14.1 (2012), pp. 90–93.

[27] Xiaoying Sun et al. “Nonphotochemical laser-induced nucleation of nematic phase and alignment of nematic director from a supercooled thermotropic liquid crystal”. In: *Physical Review E* 79.2 (2009), p. 021701.

[28] Brandon C Knott et al. “Communication: Bubbles, crystals, and laser-induced nucleation”. In: *The Journal of chemical physics* 134.17 (2011), p. 171102.

[29] Martin R Ward et al. “Laser-induced nucleation of carbon dioxide bubbles”. In: *The Journal of chemical physics* 142.14 (2015), p. 144501.

F

[30] Martin R Ward, Alasdair M Mackenzie, and Andrew J Alexander. "Role of impurity nanoparticles in laser-induced nucleation of ammonium chloride". In: *Crystal Growth & Design* 16.12 (2016), pp. 6790–6796.

[31] Yao Liu, Mees H Van Den Berg, and Andrew J Alexander. "Supersaturation dependence of glycine polymorphism using laser-induced nucleation, sonocrystallization and nucleation by mechanical shock". In: *Physical Chemistry Chemical Physics* 19.29 (2017), pp. 19386–19392.

[32] Andrew J Alexander and Philip J Camp. "Single pulse, single crystal laser-induced nucleation of potassium chloride". In: *Crystal Growth and Design* 9.2 (2009), pp. 958–963.

[33] Jelena Matic et al. "Intensity, wavelength, and polarization dependence of nonphotochemical laser-induced nucleation in supersaturated aqueous urea solutions". In: *Crystal growth & design* 5.4 (2005), pp. 1565–1567.

[34] Rohit Kacker et al. "Multiparameter investigation of laser-induced nucleation of supersaturated aqueous KCl solutions". In: *Crystal Growth & Design* 18.1 (2018), pp. 312–317.

[35] Carla Duffus, Philip J Camp, and Andrew J Alexander. "Spatial control of crystal nucleation in agarose gel". In: *Journal of the American Chemical Society* 131.33 (2009), pp. 11676–11677.

[36] Tianyi Hua et al. "Microfluidic laser-induced nucleation of supersaturated aqueous KCl solutions". In: *Crystal Growth & Design* 19.6 (2019), pp. 3491–3497.

[37] Sanjana Dhingra. "Understanding Non-Photochemical Laser Induced Nucleation". MA thesis. Delft University of Technology, 2017.

[38] Brandon C Knott, Michael F Doherty, and Baron Peters. "A simulation test of the optical Kerr mechanism for laser-induced nucleation". In: *The Journal of chemical physics* 134.15 (2011), p. 154501.

[39] Allan Myerson. *Handbook of industrial crystallization*. Butterworth-Heinemann, 2002.

[40] Joel Bernstein. *Polymorphism in Molecular Crystals 2e*. Vol. 30. International Union of Crystal, 2020.

[41] EV Boldyreva et al. "Polymorphism of glycine, Part I". In: *Journal of thermal analysis and calorimetry* 73.2 (2003), pp. 409–418.

[42] Bruce A Garetz, Jelena Matic, and Allan S Myerson. "Polarization switching of crystal structure in the nonphotochemical light-induced nucleation of supersaturated aqueous glycine solutions". In: *Physical review letters* 89.17 (2002), p. 175501.

[43] Daniel Irimia et al. "Influence of laser parameters and experimental conditions on nonphotochemical laser-induced nucleation of glycine polymorphs". In: *Crystal Growth & Design* 21.1 (2020), pp. 631–641.

[44] John C Bischof and Kenneth R Diller. "From Nanoparticle Heating to Thermoregulation: A Multiscale Bioheat Transfer Review". In: *Annual review of biomedical engineering* 20 (2018), p. 301.

F

[45] Niklas Hidman et al. “Numerical Frameworks for Laser-Induced Cavitation: Is Interface Supersaturation a Plausible Primary Nucleation Mechanism?” In: *Crystal Growth & Design* 20.11 (2020), pp. 7276–7290.

[46] W Koechner and M Bass. “Solid-State Lasers: A Graduate Text, 314 Springer Verlag”. In: *New York* (2003).

[47] Harry Nyquist. “Certain topics in telegraph transmission theory”. In: *Transactions of the American Institute of Electrical Engineers* 47.2 (1928), pp. 617–644.

[48] RW Shearman and Alan WC Menzies. “The solubilities of potassium chloride in deuterium water and in ordinary water from 0 to 180”. In: *Journal of the American Chemical Society* 59.1 (1937), pp. 185–186.

[49] Arthur A Sunier and James Baumbach. “The solubility of potassium chloride in ordinary and heavy water”. In: *Journal of Chemical and Engineering Data* 21.3 (1976), pp. 335–336.

[50] Paula Sousa and Ana MC Lopes. “Solubilities of potassium hydrogen tartrate and potassium chloride in water+ ethanol mixtures”. In: *Journal of Chemical & Engineering Data* 46.6 (2001), pp. 1362–1364.

[51] Ed Zwaan et al. “Controlled cavitation in microfluidic systems”. In: *Physical review letters* 98.25 (2007), p. 254501.

[52] Chao Sun et al. “Growth and collapse of a vapour bubble in a microtube: the role of thermal effects”. In: *Journal of fluid mechanics* 632 (2009), pp. 5–16.

[53] Henrik Bruus. *Theoretical microfluidics*. Vol. 18. Oxford university press, 2007.

[54] Anamaria Soare et al. “Crystal nucleation by laser-induced cavitation”. In: *Crystal growth & design* 11.6 (2011), pp. 2311–2316.

[55] Douglas A Skoog et al. *Fundamentals of analytical chemistry*. Cengage learning, 2013.

[56] Silvestre Roberto Gonzalez Avila, Chaolong Song, and Claus-Dieter Ohl. “Fast transient microjets induced by hemispherical cavitation bubbles”. In: *Journal of Fluid Mechanics* 767 (2015), pp. 31–51.

[57] Pedro A Quinto-Su, Kang Y Lim, and Claus-Dieter Ohl. “Cavitation bubble dynamics in microfluidic gaps of variable height”. In: *Physical Review E* 80.4 (2009), p. 047301.

[58] Werner Lauterborn and Thomas Kurz. “Physics of bubble oscillations”. In: *Reports on progress in physics* 73.10 (2010), p. 106501.

[59] Lord Rayleigh. “VIII. On the pressure developed in a liquid during the collapse of a spherical cavity”. In: *The London, Edinburgh, and Dublin Philosophical Magazine and Journal of Science* 34.200 (1917), pp. 94–98.

[60] Kaustubh R Rau et al. “Pulsed laser microbeam-induced cell lysis: time-resolved imaging and analysis of hydrodynamic effects”. In: *Biophysical journal* 91.1 (2006), pp. 317–329.